Universidade Federal do Rio Grande do Sul
Instituto de Física



Sensoriamento quântico de rotações com um modelo integrável de quatro poços

Joel Bacellar Neves

Dissertação submetida ao Programa de Pós-Graduação em Física da Universidade Federal do Rio Grande do Sul em conformidade com os requisitos parciais para a obtenção do título de Mestre em Física.

Orientadora: Angela Foerster
Coorientador: Leandro Hayato Ymai

Porto Alegre
Agosto de 2026

Resumo

Neste trabalho, apresentamos um modelo integrável de quatro poços que descreve a interação e o tunelamento de bósons dipolares ultrafrios aprisionados em uma configuração tetraédrica em rotação. O modelo é derivado de uma extensão do modelo de Bose-Hubbard em rotação, no qual os parâmetros de interação e tunelamento foram apropriadamente escolhidos para produzir quatro quantidades conservadas e independentes, estabelecendo integrabilidade. Duas dessas quantidades — relacionadas aos dois modos de circulação não nulos encontrados no sistema — são utilizadas para derivar um Hamiltoniano efetivo dinamicamente equivalente ao sistema no regime de forte interação, permitindo o estudo analítico de sua dinâmica. Ao analisar a dinâmica de ocupação dos poços no regime de forte interação, observamos que a rotação induz um desbalanço populacional entre os poços de forma semelhante ao efeito Sagnac. Esse fenômeno é explorado para construir um protocolo simples de sensoriamento capaz de estimar a rotação no sistema por medições do desbalanço populacional entre os poços. Ao calcularmos a sensibilidade do protocolo proposto, demonstramos que ele apresenta uma vantagem de escala devido a uma manifestação não trivial da não linearidade do sistema, viabilizada pela integrabilidade. Os resultados deste trabalho abrem o caminho para futuras investigações sobre os efeitos da rotação em modelos integráveis de multi-poços, destacando seu grande potencial na modelagem de sensores e dispositivos quânticos.

Palavras-chave: átomos frios, integrabilidade quântica, metrologia quântica.

Nota de imprensa

Nesta dissertação, nós investigamos um sensor quântico de rotações baseado em um modelo integrável para átomos ultrafrios. O design do sensor apresenta um protocolo simples baseado na medição de populações atômicas em uma armadilha de poços de potencial.

Desde a sua concepção, a mecânica quântica, através de uma descrição da natureza do ponto de vista de funções de onda e grandezas físicas discretas, tem nos permitido entender cada vez melhor o mundo em que vivemos. Por mais distante do dia-a-dia que a mecânica quântica possa parecer, seus conceitos estão profundamente enraizados na vida moderna. Não é preciso procurar além dos nossos celulares, que não existiriam sem os transistores, ou dos exames médicos modernos, como os raios-X, PET scans e a ressonância magnética, para encontrarmos exemplos concretos da aplicação de fenômenos quânticos. Essas e muitas outras tecnologias que existem graças ao estudo fundamental da mecânica quântica, mostram o quão importante é a "ciência de base" para o desenvolvimento tecnológico.

Dentre as diversas previsões da mecânica quântica, a condensação de Bose-Einstein é uma das mais importantes nesse contexto. Esse fenômeno, previsto há mais de um século, ocorre quando um gás de átomos "bosônicos" (átomos com spin total inteiro) é resfriado a temperaturas próximas do zero absoluto. Nessas condições, os átomos deixam de se comportar como partículas localizadas e passam a ocupar coletivamente um único estado quântico – o condensado. Isso permite o estudo em escala macroscópica de diversos fenômenos quânticos. A primeira observação experimental da condensação de Bose-Einstein, há mais de 30 anos, impulsionou o desenvolvimento de inúmeras técnicas para se resfriar, aprisionar e manipular esses "átomos ultrafrios". Atualmente, devido ao enorme controle com o qual esses sistemas podem ser criados, átomos ultrafrios se tornaram uma plataforma ideal para simular outros sistemas físicos, estudar novas teorias e medir grandezas físicas com alta precisão.

O "modelo integrável de quatro poços" explorado nesta dissertação descreve um caso particular desses sistemas. Ele considera um gás polarizado de átomos ultrafrios, aprisionados em quatro poços de potencial (pequenas armadilhas de átomos formadas pela superposição de campos eletromagnéticos). Esses poços formam os vértices de um tetraedro onde os átomos podem "tunelar" de um poço para o outro e interagir por forças de contato e interações dipolo-dipolo (de longa distância). O modelo explorado apresenta uma propriedade chamada de integrabilidade, obtida através do balanceamento da interação de contato e interação dipolo-dipolo. Sistemas integráveis possuem o mesmo número de grandezas físicas constantes ao longo do tempo (como energia, número de partículas, etc) que graus de liberdade (o menor número de parâmetros necessários para caracterizar todo o sistema). Essa propriedade permite encontrarmos soluções analíticas para o sistema, o que facilita bastante o seu estudo. Isso torna a integrabilidade uma propriedade muito vantajosa para o estudo de átomos ultrafrios e o desenvolvimento de dispositivos quânticos.

Baseando-se nisso, através do estudo da dinâmica das populações atômicas no modelo, foi identificado que o tunelamento dos átomos é favorecido no sentido de rotação quando o sistema é colocado em um referencial em rotação. Isso causa um desequilíbrio entre as populações dos poços que pode ser medido para estimar a rotação no sistema. A partir do cálculo da sensibilidade desse procedimento,

foi identificado que esse sensor apresenta uma vantagem de escala de sensibilidade devido a um mecanismo especial viabilizado pela integrabilidade do sistema.

O modelo explorado nesta dissertação faz parte de uma família maior de modelos integráveis, que até então não foram estudados em grande detalhe em referenciais com rotação. Portanto, este trabalho fornece uma base sólida para o estudo de modelos integráveis em rotação no contexto da metrologia. Assim, nossos resultados mostram o quão interessante é a integrabilidade para o estudo de átomos ultrafrios e abrem caminho para o desenvolvimento de novos dispositivos e sensores quânticos.

Contato

Joel Bacellar Neves
Instituto de Física, Universidade Federal do Rio Grande do Sul
Email: joelbacellar@gmail.com

Angela Foerster
Instituto de Física, Universidade Federal do Rio Grande do Sul
Email: angela@if.ufrgs.br

Leandro Hayato Ymai
Instituto de Física, Universidade Federal do Pampa
Email: leandroymai@unipampa.edu.br

Joel Bacellar Neves

Quantum rotation sensing with a four-site integrable model

Dissertation submitted to the Graduate Program in Physics at the Federal University of Rio Grande do Sul in partial fulfillment of the requirements for the degree of Master in Physics.

Advisor: Angela Foerster
Co-advisor: Leandro Hayato Ymai

Porto Alegre
August 2026

Abstract

In this work, we present a four-site integrable model that describes the interaction and tunneling of ultracold dipolar bosons trapped in a rotating, tetrahedral site arrangement. The model is derived from an extension of the Bose-Hubbard model in a rotating frame where the interaction and tunneling parameters have been appropriately selected to produce four independent and conserved quantities, establishing integrability. Two of these conserved quantities – related to the two nonzero circulation modes found in the system – are used to derive an effective Hamiltonian dynamically equivalent to the system for large interactions, allowing for the analytical prediction of its quantum dynamics. By analyzing the site population dynamics in this large interaction regime, we find that rotation induces population imbalance in a manner akin to the Sagnac effect. This is exploited to design a simple rotation sensing protocol capable of estimating reference frame rotation through population imbalance measurements. We calculate the sensitivity of the proposed protocol and demonstrate it has a scaling advantage due to a nontrivial manifestation of the system's nonlinearity, enabled by integrability. The findings presented here open further investigations into the effects of rotation in multi-site integrable models, highlighting their great potential for modeling quantum devices and quantum sensors.

Key-words: cold atoms, quantum integrability, quantum metrology.

Contents

1 Introduction **4**

2 Four-site integrable model **6**
2.1 Integrable Hamiltonian 6
2.2 Resonant regime 8
2.3 Rotation sensing 9

3 Theoretical framework **10**
3.1 Extended Bose-Hubbard Hamiltonian 10
3.2 Four-site Hamiltonian 12
3.2.1 Cubic lattice geometry 12
3.2.2 Interaction Parameters 13
3.2.3 Rotating frame 14
3.3 Conserved quantities 15
3.4 Quantum dynamics 17
3.5 Effective Hamiltonian 19

4 Quantum rotation sensor **21**
4.1 Quantum metrology 21
4.2 Quantum dynamics under rotation 25
4.3 Optimal rotation sensing bounds 27
4.4 Rotation sensing protocol 28

5 Conclusion **31**

A Analytical formulae **33**
A.1 Second-order transition rates 33
A.2 Initial state evolution 34
A.3 Outer site expectation values 35
A.4 Error formula calculation 36

Bibliography **38**

Chapter 1

Introduction

Bose-Einstein condensation is a phase transition encountered in bosonic many-body systems characterized by the macroscopic occupation of a single quantum state – the condensate. This phenomenon is a direct consequence of the statistical distribution of bosons (particles with integer spin and symmetric wavefunctions under particle exchange) and occurs when a bosonic ensemble is cooled down below temperatures close to absolute zero, where the thermal wavelength of its particles becomes larger than the average distance between them. Since its theoretical prediction during 1924-1925 in a series of papers by Einstein [1, 2] crediting the work of the indian physicist Satyendra Nath Bose [3], Bose-Einstein condensation has shaped physics research over many distinct areas for more than a century.

The first experimental realization of a Bose-Einstein condensate (BEC) in a weakly interacting dilute gas, in the labs of Cornell/Wieman [4] and Ketterle [5] in 1995, sparked a new wave of experimental interest surrounding cold atomic systems, which led to the rapid development of techniques to cool, confine and manipulate atoms. Not long after, experiments with Feshbach resonances [6, 7], which allow the modification of the s-wave scattering length to large values, and optical lattices [8] allowed experimentalists to explore the physical realization of strongly interacting and strongly correlated cold atom systems. Since the usual mean-field methods based on the Gross-Pitaevskii and Bogoliubov equations, which provide very accurate physical descriptions for most weakly interacting cold atom systems [9, 10], cease to do so in strong interaction regimes, this development prompted a resurgence in beyond mean-field and number-conserving approaches, like the Bose-Hubbard model (BHM) and its extensions.

The BHM describes the on-site interaction and nearest-neighbor tunneling of bosons trapped in lattice systems. It was first derived by Gersch and Knollman in 1963 [11], prior to Hubbard's iconic fermionic counterpart [12]. When other interactions between particles are considered, e.g. the dipole-dipole interaction (DDI), the model is often referred to as a nonstandard or extended Bose-Hubbard model (EBHM). The BHM became specially relevant after optical lattice technology enabled the observation of the Superfluid to Mott Insulator (SF-MI) transition in a cold atom gas in 2002 [8]. This result, predicted in 1998 [13], marked the first experimental realization of the BHM and, since then, the model and its extensions have been extensively studied and used to successfully describe many experiments of ultracold atoms in optical lattices [14–18].

Optical lattices provide practically ideal, loss-free potentials in which ultracold atoms may move and interact with one another [19, 20], thus making ultracold atoms in optical lattices an excellent platform for quantum simulation, atomtronics and precision metrology. When considering dipolar bosons in optical lattices, the additional long-range DDI enables a new range of dynamical regimes and quantum phase-transitions, which have been thoroughly described by EBHMs (for recent reviews, see [17, 18]).

Thus far, a number of EBHMs used to describe ultracold dipolar bosons trapped in finite lattice arrangements have been shown to have integrable regimes [21–28], characterized by the existence of as many independent and conserved quantities as degrees of freedom [29, 30]. These conservation laws impose constraints to the accessible Hilbert space, leading to an orderly dynamics that can be analytically solved through extensions of the quantum inverse scattering method (QISM) [22] or other approaches. This feature can be highly advantageous and has been exploited to design atomtronic quantum devices and precision metrology protocols with ultracold atoms [23–28].

Motivated by the research surrounding integrable models and the field of quantum metrology, in this work we present the design of a quantum rotation sensing protocol based on a four-site integrable model in a rotating frame [31]. The studied model is part of a larger family of multi-site integrable models [22], which until now have only been studied in non-rotating, static frames. This dissertation was written with the goal of supporting further research into the effects of rotation in multi-site integrable models and providing a generalist overview of quantum metrology for those not familiar with the area. The discussion is structured as follows:

- Chapter 2 provides an overview of the four-site integrable model;
- Chapter 3 provides a comprehensive description of the model's theoretical framework;
- Chapter 4 provides an overview of quantum metrology and goes over the application of the model as a quantum rotation sensor;
- Chapter 5 synthesizes the main results and conclusions of the dissertation.

Chapter 2

Four-site integrable model

In this chapter, we provide a general introduction to the four-site integrable model discussed throughout this work, going over its Hamiltonian, conserved quantities, relevant dynamical regimes and possible applications in quantum metrology. The numerical evaluation of quantities related to the system's dynamics was performed using a Python program developed by the authors[1].

2.1 Integrable Hamiltonian

This work focuses on a particular cold atom system, where the interaction parameters are appropriately selected to produce a four-site integrable model. The system consists of an ensemble of ultracold dipolar bosons trapped in trirectangular tetrahedral site arrangement, with a central site (labeled 4) connected to three outer sites (labeled 1, 2 and 3), in a rotating frame with constant angular velocity $\mathbf{\Omega} = \Omega\hat{z}$. Figure 2.1 provides a schematic representation of the model.

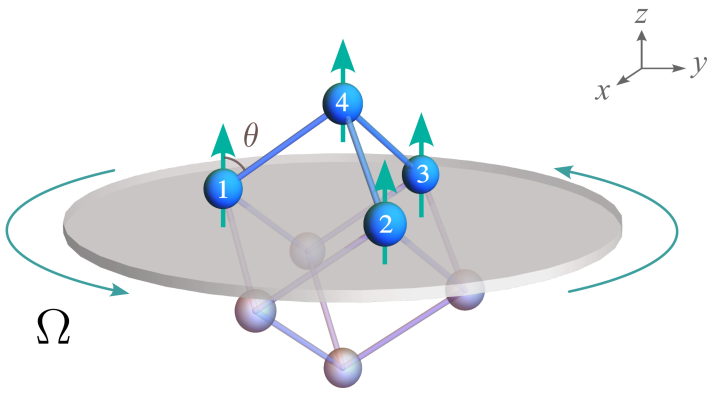

Figure 2.1: Schematic figure of the system. The four-site geometry is derived from a tilted cubic optical lattice confined by an external field (not shown). The cyan arrows represent the dipoles aligned along the z axis. The circulating arrow represents $\mathbf{\Omega} = \Omega\hat{z}$.

[1] https://github.com/joel-b-neves/masters-dissertation-programs-2026

The four-site integrable model is derived from an extension of the Bose-Hubbard model in a rotating frame. Extended Bose-Hubbard models (EBHM) describe the interaction and nearest-neighbor tunneling of bosons trapped in lattice systems. They include both on-site and off-site interactions, the latter usually in the form of long-range electric or magnetic dipole-dipole interactions (DDI). The EBHM Hamiltonian for a fixed number of particles and isotropic tunneling can be written as

$$H = \frac{U_0}{2}\sum_i N_i\left(N_i - 1\right) + \sum_{i\neq j}\frac{U_{ij}}{2}N_iN_j + \sum_i \nu_i N_i - J\sum_{\langle i,j\rangle}\left(a_i^\dagger a_j + a_j^\dagger a_i\right) \tag{2.1}$$

where U_0 is the on-site interaction between atoms, $a_i^\dagger$, a_i and $N_i = a_i^\dagger a_i$ are the bosonic creation, annihilation and number operators at the i-th site, U_{ij} is the long-range interaction between sites i and j, ν_i is the energy of an external field at i-th site, and J is the hopping rate between nearest-neighbor sites – indicated by the $\langle i, j\rangle$ sum notation.

To derive the four-site integrable Hamiltonian, we assume all dipoles to be polarized along the z axis. The four-site geometry is realized by confining the unit cell of a cubic optical lattice using an external harmonic potential (see figure 2.1). Integrability is then achieved by balancing the on-site interaction to cancel out the long-range interaction of the outer sites ($U_0 = U_{12} = U_{23} = U_{31}$). Finally, we transform the system to a rotating frame with constant angular velocity $\mathbf{\Omega} = \Omega\hat{z}$, leading to the four-site integrable Hamiltonian:

$$H = U\left(N - 2N_4\right)^2 + \nu\left(N - 2N_4\right) - J\sum_{i=1}^{3}\left(a_i^\dagger a_4 + a_4^\dagger a_i\right) - \zeta\mathcal{J}. \tag{2.2}$$

In the above expression, $U = U_0/4$ is the effective on-site interaction energy, ν characterizes the interaction energy due to the external harmonic potential used to confine the system, $\zeta = W\Omega$ is the rotational energy due to the frame's angular velocity, where W is the angular quasimomentum defined in Section 3.2.3, and $\mathcal{J}$ is a current operator related to the second quantization of angular momentum in the four-site occupancy basis:

$$\mathcal{J} = -\frac{i}{\sqrt{3}}\left(a_1^\dagger a_2 + a_2^\dagger a_3 + a_3^\dagger a_1 - a_2^\dagger a_1 - a_1^\dagger a_3 - a_3^\dagger a_2\right). \tag{2.3}$$

The four-site integrable model has four independent and conserved quantities. Besides the Hamiltonian and the total number of particles (H and N), we have two additional nontrivial conserved quantities, referred to as "conserved charges":

$$\begin{aligned} Q_+ = \frac{1}{3}\Big[&N_1 + N_2 + N_3 \\ &+e^{-2\pi i/3}\left(a_1^\dagger a_2 + a_2^\dagger a_3 + a_3^\dagger a_1\right) + e^{2\pi i/3}\left(a_1^\dagger a_3 + a_3^\dagger a_2 + a_2^\dagger a_1\right)\Big], \\ Q_- = \frac{1}{3}\Big[&N_1 + N_2 + N_3 \\ &+e^{2\pi i/3}\left(a_1^\dagger a_2 + a_2^\dagger a_3 + a_3^\dagger a_1\right) + e^{-2\pi i/3}\left(a_1^\dagger a_3 + a_3^\dagger a_2 + a_2^\dagger a_1\right)\Big], \end{aligned} \tag{2.4}$$

which satisfy $[H, Q_\pm] = [N, Q_\pm] = [Q_+, Q_-] = 0$, such that the system has four degrees of freedom and four algebraically independent conserved operators, establishing integrability [22, 29, 30]. Equation (2.4) shows that the conserved charges

are related to clockwise (Q_-) and counterclockwise (Q_+) tunneling along the outer sites of the system, due to their circular tunneling structure. They are obtained through the exact diagonalization of the current operator, such that

$$\mathcal{J} = Q_+ - Q_-, \tag{2.5}$$

and can be thought of as the occupation numbers of the two nonzero circulation modes found in the system. These quantities can be used in the description of an effective Hamiltonian for the strong interaction regime of the system, allowing for the analytical prediction of the system's quantum dynamics.

2.2 Resonant regime

The four-site integrable model can achieve different dynamical regimes depending on the current ratio between interaction strength and tunneling amplitude in the system. These regimes can be characterized by

$$\chi = \left| \frac{U\left(N - 2k\right) + \nu/2}{J} \right|, \tag{2.6}$$

where k is the central site's initial population. For the purposes of this work, we will mainly focus on the strong interaction regime of the system, referred to as "resonant tunneling" regime, where the interaction parameters dominate the tunneling dynamics ($\chi \gg 1$).

In the resonant regime, tunneling occurs as if the central and outer sites were two isolated, noninteracting subsystems. This behavior results from the the interaction driven tilts $U\left(N - 2N_4\right)^2$ and $\nu\left(N - 2N_4\right)$ of Hamiltonian (2.2), which tend to confine the atoms to their initial subsystems as χ increases, and the absence of long-range interaction between the outer sites due to the integrability condition, which transforms the outer sites into an effectively noninteracting subsystem, where atoms can tunnel freely via a second-order process through the central site [32]. As a result, outer site populations exhibit harmonic oscillations, while $\langle N_1 + N_2 + N_3 \rangle$ and $\langle N_4 \rangle$ remain constant over time.

By treating the tunneling terms of Hamiltonian (2.2) as a weak physical disturbance in the strong interaction regime, we can calculate the effective tunneling amplitude of the second-order processes through the central site. This allows for an effective Hamiltonian dynamically equivalent to the resonant regime to be derived:

$$H_{\text{eff}} = -\left(\xi + \zeta\right) Q_+ - \left(\xi - \zeta\right) Q_- \tag{2.7}$$

where

$$\xi = \frac{3J^2}{4U}\left(\frac{k+1}{N - 2k - 1 + \frac{\nu}{2U}} - \frac{k}{N - 2k + 1 + \frac{\nu}{2U}}\right). \tag{2.8}$$

The effective Hamiltonian provides a better lens through which to analyze the resonant regime, and allows us to derive analytical expressions for the time evolution of the outer site populations. The most important takeaway from Equation (2.7) is that rotation imposes a direct imbalance between Q_+ and Q_-, which can be exploited to design a rotation sensor out of the model. This is discussed in more detail in the next section.

2.3 Rotation sensing

The four-site integrable model's main application, as a quantum device, is rotation sensing, due to the effect rotation has on the tunneling dynamics of the system. Here we present this result by summarizing the findings of Sections (3.2.3), (4.2) and (4.4).

By transforming Equation (2.1) from its stationary frame to a rotating frame, through the action of $\hat{U}(t) = \exp(it\Omega\hat{L}_z)$ (in units with $\hbar = 1$), one finds that rotation manifests as induced tunneling in the system. This can be seen in the current operator $\mathcal{J} = Q_+ - Q_-$ found in Hamiltonian (2.2). Recalling the physical interpretation of Q_+ and Q_- as the occupation numbers of counterclockwise and clockwise circulation, it's easy to see that tunneling is skewed towards the direction of rotation as angular velocity increases. This is akin to the phase shift induced by reference frame rotation in the Sagnac Effect [33]. This effect becomes really apparent in the resonant regime, since rotation-induced tunneling can easily overpower nearest-neighbor tunneling in this regime, while the underlying harmonic dynamics of the outer site populations remains unaffected by rotation.

As stated in the previous section, the effective Hamiltonian can be leveraged to derive analytical expressions for the expectation values of the outer site populations in the resonant regime. This can be achieved by evaluating the quantum dynamics of the system through the action of $\hat{U}(t) = \exp(-itH_{\text{eff}})$. By doing so for an initial state where all atoms occupy one of the outer sites, we find that at $t = \tau \equiv \pi/\xi$ there is a one-to-one rotation-to-imbalance correspondence for rotation speeds in the interval $|\zeta| \leq \xi/3$, where increasing angular velocity directly increases the population imbalance between the two initially unoccupied sites. This feature was thoroughly exploited in Chapter 4 to design a quantum rotation sensor out of the model, capable of estimating reference frame rotation through site population measurements.

Chapter 3

Theoretical framework

This chapter provides a comprehensive description of the model's theoretical framework and a detailed study of its dynamics. We start by deriving an extension of the Bose-Hubbard Hamiltonian for an ensemble of polarized ultracold magnetic atoms, from which we gradually outline the four-site integrable model in the subsequent sections.

3.1 Extended Bose-Hubbard Hamiltonian

Let's consider a system of N bosons trapped in an isotropic lattice potential V_{lat} confined by an external field V_{ext}, where the total number of particles is conserved. A good jumping point is to start from the general second quantization Hamiltonian for a Bose gas [10]

$$\begin{aligned}\hat{H} = &\int d\boldsymbol{r}\hat{\Psi}^{\dagger}(\boldsymbol{r},t)\,\hat{h}_0(\boldsymbol{r})\,\hat{\Psi}(\boldsymbol{r},t)\\ &+\frac{1}{2}\int\int d\boldsymbol{r}d\boldsymbol{r}'\hat{\Psi}^{\dagger}(\boldsymbol{r},t)\,\hat{\Psi}^{\dagger}(\boldsymbol{r}',t)\,V(\boldsymbol{r}-\boldsymbol{r}')\,\hat{\Psi}(\boldsymbol{r}',t)\,\hat{\Psi}(\boldsymbol{r},t)\end{aligned} \tag{3.1}$$

where

$$\hat{h}_0(\boldsymbol{r}) = -\frac{\hbar^2}{2m}\nabla^2 + V_{\text{lat}}(\boldsymbol{r}) + V_{\text{ext}}(\boldsymbol{r}) \tag{3.2}$$

is the single-particle Hamiltonian found in the Schroedinger equation, m is the atomic species mass, $V(\boldsymbol{r}-\boldsymbol{r}')$ is the exact two-body interatomic potential, and $\hat{\Psi}^{\dagger}$ and $\hat{\Psi}$ are the so-called creation and annihilation Bose field operators. One can picture $\hat{\Psi}^{\dagger}$ as the addition of a particle at position $\boldsymbol{r}$ and time t and $\hat{\Psi}$ as its removal, hence their names.

The two-body interatomic potential for a dipolar Bose gas at very low temperature is

$$V(\boldsymbol{r}-\boldsymbol{r}') = g\delta(\boldsymbol{r}-\boldsymbol{r}') + V_{dd}(\boldsymbol{r}-\boldsymbol{r}')\,. \tag{3.3}$$

The first part is the contact interaction between the atoms, where the interaction strength $g = 4\pi\hbar^2 a/m$ is characterized by the atomic species s-wave scattering length a, which can be tuned via Feshbach resonance [6, 7]. The second part is the two-body dipole-dipole interaction potential. For two particles at positions $\boldsymbol{r}$ and $\boldsymbol{r}'$, with dipole moments along the unit vectors $\boldsymbol{e}_1$ and $\boldsymbol{e}_2$, it reads

$$V_{dd}(\boldsymbol{r}-\boldsymbol{r}') = \frac{C_{dd}}{4\pi}\frac{(\boldsymbol{e}_1\cdot\boldsymbol{e}_2)\,|\boldsymbol{r}-\boldsymbol{r}'|^2 - 3\,[\boldsymbol{e}_1\cdot(\boldsymbol{r}-\boldsymbol{r}')]\,[\boldsymbol{e}_2\cdot(\boldsymbol{r}-\boldsymbol{r}')]}{|\boldsymbol{r}-\boldsymbol{r}'|^5}. \tag{3.4}$$

For particles with permanent magnetic dipole p, the coupling constant C_{dd} is $\mu_0 p^2$, where μ_0 is the permeability of vacuum. We consider an ensemble where all dipoles are polarized along the z axis by an external magnetic field, so Equation (3.4) simplifies to

$$V_{dd}(\boldsymbol{r}-\boldsymbol{r}') = \frac{C_{dd}}{4\pi}\frac{(1-3\cos^2\theta)}{|\boldsymbol{r}-\boldsymbol{r}'|^3}, \tag{3.5}$$

where θ is the angle between the direction of polarization and $\boldsymbol{r}-\boldsymbol{r}'$.

In an ultracold regime where all atoms are considered to be in their lowest possible energy state, the field operators become a sum over the ground states at each site [10, 34]:

$$\hat{\Psi}(\boldsymbol{r}) = \sum_i a_i \varphi_0(\boldsymbol{r}-\boldsymbol{r}_i), \quad \hat{\Psi}^\dagger(\boldsymbol{r}) = \sum_i a_i^\dagger \varphi_0^*(\boldsymbol{r}-\boldsymbol{r}_i), \tag{3.6}$$

where $\boldsymbol{r}_i = (x_i, y_i, z_i)$ is the position of the i-th site and $\varphi_0(\boldsymbol{r}-\boldsymbol{r}_i)$ is its lowest Bloch band Wannier function (where t is omitted for brevity). Substituting for $\hat{\Psi}^\dagger(\boldsymbol{r})$, $\hat{\Psi}(\boldsymbol{r})$ and $V(\boldsymbol{r}-\boldsymbol{r}')$ in Equation (3.1) yields the extended Bose-Hubbard Hamiltonian [35, 36]:

$$H = \frac{U_0}{2}\sum_i N_i(N_i-1) + \sum_{i\neq j}\frac{U_{ij}}{2}N_iN_j + \sum_i \nu_i N_i - J\sum_{\langle i,j\rangle}\left(a_i^\dagger a_j + a_j^\dagger a_i\right) \tag{3.7}$$

where

$$\begin{aligned} U_0 &= g\int d\boldsymbol{r}\,|\varphi_0(\boldsymbol{r}-\boldsymbol{r}_i)|^4 \\ &\quad + \int\int d\boldsymbol{r}d\boldsymbol{r}'\,|\varphi_0(\boldsymbol{r}-\boldsymbol{r}_i)|^2 V_{dd}(\boldsymbol{r}-\boldsymbol{r}')\,|\varphi_0(\boldsymbol{r}'-\boldsymbol{r}_i)|^2 \end{aligned} \tag{3.8}$$

is the on-site interaction energy found in Equation (2.1), which includes both contact interaction and on-site magnetic DDI contributions,

$$U_{ij} = \int\int d\boldsymbol{r}d\boldsymbol{r}'\,|\varphi_0(\boldsymbol{r}-\boldsymbol{r}_i)|^2 V_{dd}(\boldsymbol{r}-\boldsymbol{r}')\,|\varphi_0(\boldsymbol{r}'-\boldsymbol{r}_j)|^2 \tag{3.9}$$

is the off-site interaction energy from the magnetic DDI between sites i and j,

$$\nu_i = \int d\boldsymbol{r}\,|\varphi_0(\boldsymbol{r}-\boldsymbol{r}_i)|^2 V_{\text{ext}}(\boldsymbol{r}) \tag{3.10}$$

is the external field energy at site i, and

$$J = -\int d\boldsymbol{r}\varphi_0^*(\boldsymbol{r}-\boldsymbol{r}_i)\left[-\frac{\hbar^2}{2m}\nabla^2 + V_{\text{lat}}(\boldsymbol{r})\right]\varphi_0(\boldsymbol{r}-\boldsymbol{r}_j) \tag{3.11}$$

is the hopping rate between nearest-neighbor sites, which is independent of nearest-neighbor choice due to V_{lat} being isotropic. As expected, Equation (3.7) reduces to the standard Bose-Hubbard Hamiltonian when $V_{dd} \to 0$, and the Hamiltonian H and total particle number N commute and are trivial independent and conserved quantities of the system.

3.2 Four-site Hamiltonian

3.2.1 Cubic lattice geometry

The four-site integrable model has its geometry derived from a tilted cubic optical lattice, where the sites occupy the corner of a unit cell at its origin, forming a trirectangular tetrahedron (see figure 2.1). In this case, first-order tunneling can only occur between the central site at the tetrahedron's apex and one of the three outer sites that form its base.

This site arrangement can be realized by interfering three orthogonal standing laser fields [34] of wavelength λ and confining the sites with a harmonic potential. In the context of Equation (3.2), the trapping potential that characterizes the physical realization of the system is

$$V(\boldsymbol{r}) = V_{\text{lat}}(\boldsymbol{r}) + V_{\text{ext}}(\boldsymbol{r}). \tag{3.12}$$

The first part, which represents the isotropic lattice potential, is the tilted cubic optical lattice described by

$$V_{\text{lat}}(\boldsymbol{r}) = V_0 \sum_{i=1}^{3} \cos^2\left(\frac{\pi \boldsymbol{r}}{L} \cdot \boldsymbol{u}_i + \varphi_i\right) \tag{3.13}$$

where V_0 characterizes the lattice potential depth, $L = \lambda/2$ is the lattice length, $\varphi_1 = \varphi_2 = \pi/6$ and $\varphi_3 = 7\pi/6$, and $\boldsymbol{u}_i$ are the unit vectors

$$\begin{aligned} \boldsymbol{u}_1 &= \left(\frac{1}{\sqrt{2}}, \frac{1}{\sqrt{6}}, \frac{1}{\sqrt{3}}\right), \\ \boldsymbol{u}_2 &= \left(-\frac{1}{\sqrt{2}}, \frac{1}{\sqrt{6}}, \frac{1}{\sqrt{3}}\right), \\ \boldsymbol{u}_3 &= \left(0, -\frac{2}{\sqrt{6}}, \frac{1}{\sqrt{3}}\right). \end{aligned} \tag{3.14}$$

The second part, which represents the external field confining the system, is the harmonic potential that isolates the four-site geometry, given by

$$V_{\text{ext}}(\boldsymbol{r}) = \frac{1}{2} m \omega_{\text{ext}}^2 \left[x^2 + y^2 + (z - \Delta z)^2\right], \tag{3.15}$$

where ω_{ext} is the external trapping frequency and Δz is a small displacement above the origin, such as to isolate the sites at positions

$$\begin{aligned} \boldsymbol{r}_1 = (x_1, y_1, z_1) &= \left(-\frac{L}{\sqrt{2}}, -\frac{L}{\sqrt{6}}, 0\right), \\ \boldsymbol{r}_2 = (x_2, y_2, z_2) &= \left(\frac{L}{\sqrt{2}}, -\frac{L}{\sqrt{6}}, 0\right), \\ \boldsymbol{r}_3 = (x_3, y_3, z_3) &= \left(0, \frac{2L}{\sqrt{6}}, 0\right), \\ \boldsymbol{r}_4 = (x_4, y_4, z_4) &= \left(0, 0, \frac{L}{\sqrt{3}}\right). \end{aligned} \tag{3.16}$$

3.2.2 Interaction Parameters

The four-site Hamiltonian is obtained by calculating the interaction parameters found in Equation (3.7) after restricting it to the four-site geometry. For the nearest-neighbor tunneling terms, we simply have

$$J\sum_{\langle i,j\rangle}\left(a_i^\dagger a_j + a_j^\dagger a_i\right) = J\sum_{i=1}^{3}\left(a_i^\dagger a_4 + a_4^\dagger a_i\right). \tag{3.17}$$

The on-site interaction energy can be rearranged through a difference of squares, up to a global constant $U_0 N\left(N-2\right)/4$, into the reduced form

$$\frac{U_0}{2}\sum_{i=1}^{4} N_i\left(N_i-1\right) = \frac{U_0}{4}\left(N-2N_4\right)^2 - U_0\left(N_1N_2+N_2N_3+N_3N_1\right). \tag{3.18}$$

Because of the localization of the wavefunctions at the bottom of the sites, the off-site interaction energies described by Equation (3.9) are in good approximation given by [37],

$$U_{ij} = \frac{C_{dd}}{4\pi r_{ij}^3}\left(1-3\cos^2\theta_{ij}\right), \tag{3.19}$$

where $\boldsymbol{r}_{ij}$ is the distance between sites i and j, and θ_{ij} is the angle between $\boldsymbol{r}_{ij}$ and the orientation of the dipoles. Thus, given that in the four-site geometry we have $\cos\theta_{14} = 1/\sqrt{3}$ and $\cos\theta_{12} = 0$ for dipoles polarized in the z direction, we have

$$U_{14} = U_{24} = U_{34} = 0, \quad U_{12} = U_{23} = U_{31} = \frac{C_{dd}}{4\pi r_{12}^3}, \tag{3.20}$$

where $r_{12} = r_{23} = r_{31} = \sqrt{2}L$.

Finally, since we have $\nu_1 = \nu_2 = \nu_3$ due to the symmetry of the outer sites, substituting for Equations (3.15) and (3.16) in Equation (3.10) and assuming the Wannier functions at each site to be approximately gaussian [34] yields a total confinement energy of

$$\sum_{i=1}^{4}\nu_i N_i = \nu\left(N-2N_4\right) + \nu_0 N \tag{3.21}$$

where $\nu_0 N$ is a global constant that can be ignored and ν is the effective interaction energy due to the external harmonic field used to confine the system, given by

$$\nu = \frac{m\omega_{\text{ext}}^2 L^2}{12}\left(1+\frac{2\sqrt{3}\Delta z}{L}\right). \tag{3.22}$$

By combining Equations (3.17), (3.18), (3.20) and (3.21), we get the general, non-integrable four-site Hamiltonian that describes the system:

$$\begin{aligned} H_{\text{non-int}} = {} & \frac{U_0}{4}\left(N-2N_4\right)^2 + \left(U_{12}-U_0\right)\left(N_1N_2+N_2N_3+N_3N_1\right) \\ & + \nu\left(N-2N_4\right) - J\sum_{i=1}^{3}\left(a_i^\dagger a_4 + a_4^\dagger a_i\right) \end{aligned} \tag{3.23}$$

The integrable regime is achieved when the condition $U_{12} = U_0$ is met. This requires balancing the scattering length to cancel out the dipole-dipole interaction between the outer sites. Under these conditions, we get the stationary four-site integrable Hamiltonian:

$$H_{\text{stationary}} = U\left(N - 2N_4\right)^2 + \nu\left(N - 2N_4\right) - J\sum_{i=1}^{3}\left(a_i^\dagger a_4 + a_4^\dagger a_i\right) \tag{3.24}$$

where we define the effective interaction energy $U = U_0/4$.

3.2.3 Rotating frame

Since angular momentum is the generator of rotations, we can change (3.1) from its stationary frame to a rotating frame with constant angular velocity $\boldsymbol{\Omega}$ by applying the unitary transform

$$\hat{U}\left(t\right) = \exp\left(\frac{it}{\hbar}\boldsymbol{\Omega}\cdot\hat{\boldsymbol{L}}\right). \tag{3.25}$$

Due to the symmetry of the two-body interatomic potential, the transform affects only the single-particle Hamiltonian of Equation (3.2), changing it to

$$\hat{h}_0' = \hat{U}\hat{h}_0\hat{U}^\dagger + i\hbar\frac{\partial\hat{U}}{\partial t}\hat{U}^\dagger = \hat{h}_0\left(\boldsymbol{r}\right) - \boldsymbol{\Omega}\cdot\hat{\boldsymbol{L}}\left(\boldsymbol{r}\right). \tag{3.26}$$

Substituting for $\hat{\Psi}^\dagger$, $\hat{\Psi}$ and $\hat{h}_0'$ in Equation (3.1) now yields an additional rotational energy term, given by

$$H_\Omega = \sum_{j,k} a_j^\dagger a_k \zeta_{jk} = \sum_{j,k} a_j^\dagger a_k \left[-\int d\boldsymbol{r}\varphi_0^*\left(\boldsymbol{r} - \boldsymbol{r}_j\right)\boldsymbol{\Omega}\cdot\hat{\boldsymbol{L}}\left(\boldsymbol{r}\right)\varphi_0\left(\boldsymbol{r} - \boldsymbol{r}_k\right)\right]. \tag{3.27}$$

By analyzing Equation (3.27), we can see that rotation manifests as induced tunneling in the system, with effective amplitudes given by ζ_{jk}.

For the purposes of this work, the four-site model is analyzed in a rotating non-inertial frame with constant angular velocity $\boldsymbol{\Omega} = \Omega\hat{z}$. In this scenario, due to the four-site geometry, the induced tunneling amplitudes satisfy $\zeta_{jj} = 0$, $\zeta_{jk} = -\zeta_{kj}$, $\zeta_{14} = \zeta_{24} = \zeta_{34} = 0$ and $\zeta_{12} = \zeta_{23} = \zeta_{31}$, resulting in

$$H_\Omega = \sum_{j,k} a_j^\dagger a_k \zeta_{jk} = \frac{i\zeta}{\sqrt{3}}\left(a_1^\dagger a_2 + a_2^\dagger a_3 + a_3^\dagger a_1 - a_2^\dagger a_1 - a_1^\dagger a_3 - a_3^\dagger a_2\right) \tag{3.28}$$

where we define the rotational energy parameter

$$\zeta = -\Omega\int d\boldsymbol{r}\varphi_0^*\left(\boldsymbol{r} - \boldsymbol{r}_1\right)\hat{L}_z\varphi_0\left(\boldsymbol{r} - \boldsymbol{r}_2\right) \equiv W\Omega. \tag{3.29}$$

If we now add the rotation induced terms to the stationary Hamiltonian (3.24), we recover the rotating four-site Hamiltonian introduced in Chapter 2:

$$H = U\left(N - 2N_4\right)^2 + \nu\left(N - 2N_4\right) - J\sum_{i=1}^{3}\left(a_i^\dagger a_4 + a_4^\dagger a_i\right) - \zeta\mathcal{J} \tag{3.30}$$

where rotation induced tunneling is described by the circular current operator

$$\mathcal{J} = -\frac{i}{\sqrt{3}}\left(a_1^\dagger a_2 + a_2^\dagger a_3 + a_3^\dagger a_1 - a_2^\dagger a_1 - a_1^\dagger a_3 - a_3^\dagger a_2\right). \tag{3.31}$$

3.3 Conserved quantities

The four-site integrable model has four degrees of freedom and, therefore, must have four independent and conserved quantifies. The two trivial ones are H and N, as stated before. The remaining two, although not as trivial, are related to the rotational symmetry of the system and can be derived through the diagonalization of the current operator $\mathcal{J}$ given by Equation (3.31).

The matrix representation of $\mathcal{J}$ in the single-particle occupancy basis of the outer sites is given by:

$$\mathcal{J} = \frac{i}{\sqrt{3}} \begin{pmatrix} 0 & 1 & -1 \\ -1 & 0 & 1 \\ 1 & -1 & 0 \end{pmatrix}. \tag{3.32}$$

The matrix in Equation (3.32) is circulant and its eigenvectors are the Fourier modes $v_0 = (1,1,1)^T$, $v_+ = (1,\sigma,\sigma^{-1})^T$ and $v_- = (1,\sigma^{-1},\sigma)^T$ where $\sigma = e^{2\pi i/3}$ [38]. Thus, the single-particle eigenstates of $\mathcal{J}$ in the occupancy basis of the four sites (see Equation (3.45) for context) are:

$$\begin{aligned} |\Psi_0\rangle &= b_0^\dagger |0\rangle \equiv \frac{1}{\sqrt{3}} \left(a_1^\dagger + a_2^\dagger + a_3^\dagger\right) |0\rangle , \\ |\Psi_+\rangle &= b_+^\dagger |0\rangle \equiv \frac{1}{\sqrt{3}} \left(a_1^\dagger + \sigma a_2^\dagger + \sigma^{-1} a_3^\dagger\right) |0\rangle , \\ |\Psi_-\rangle &= b_-^\dagger |0\rangle \equiv \frac{1}{\sqrt{3}} \left(a_1^\dagger + \sigma^{-1} a_2^\dagger + \sigma a_3^\dagger\right) |0\rangle , \end{aligned} \tag{3.33}$$

where we defined the normalized modes ($m = -1, 0, 1$)

$$b_m^\dagger = \frac{1}{\sqrt{3}} \left(a_1^\dagger + \sigma^m a_2^\dagger + \sigma^{-m} a_3^\dagger\right). \tag{3.34}$$

Using the above operators, the complete set of eigenstates of $\mathcal{J}$ for a fixed total number of particles $N - k = n_0 + n_+ + n_-$, where k is the central site's initial population, can be written as

$$|n_0, n_+, n_-\rangle = \frac{(b_0^\dagger)^{n_0}}{\sqrt{n_0!}} \frac{(b_+^\dagger)^{n_+}}{\sqrt{n_+!}} \frac{(b_-^\dagger)^{n_-}}{\sqrt{n_-!}} |0\rangle . \tag{3.35}$$

The normalized modes $b_m^\dagger$ and b_m defined in Equation (3.34) represent the creation and annihilation of a quasiparticle of angular momentum in one of the three quantized circulation modes found in the system: none (0), counterclockwise (+) and clockwise (−). Since they are true creation and annihilation operators, we may associate them with their own number operators of the form $Q_m = b_m^\dagger b_m$:

$$\begin{aligned} Q_0 &= \frac{1}{3}\Big(N_1 + N_2 + N_3 \\ &\qquad + a_1^\dagger a_2 + a_2^\dagger a_3 + a_3^\dagger a_1 + a_1^\dagger a_3 + a_3^\dagger a_2 + a_2^\dagger a_1\Big) \\ Q_+ &= \frac{1}{3}\Big[N_1 + N_2 + N_3 \\ &\qquad + \sigma^{-1}\left(a_1^\dagger a_2 + a_2^\dagger a_3 + a_3^\dagger a_1\right) + \sigma\left(a_1^\dagger a_3 + a_3^\dagger a_2 + a_2^\dagger a_1\right)\Big] \\ Q_- &= \frac{1}{3}\Big[N_1 + N_2 + N_3 \\ &\qquad + \sigma\left(a_1^\dagger a_2 + a_2^\dagger a_3 + a_3^\dagger a_1\right) + \sigma^{-1}\left(a_1^\dagger a_3 + a_3^\dagger a_2 + a_2^\dagger a_1\right)\Big] \end{aligned} \tag{3.36}$$

By construction, the number operators of (3.36), hereby referred to as "charge" operators, follow the usual commutation relations of the bosonic creation, annihilation and number operators, and represent the occupancy of each of the three aforementioned modes of circulation. By combining their expressions, we observe that, as expected, their sum yields the total number of particles in the outer sites,

$$Q_0 + Q_+ + Q_- = N_1 + N_2 + N_3, \tag{3.37}$$

and that Q_+ and Q_- are related to the second-quantization of angular momentum in the system:

$$Q_+ - Q_- = \mathcal{J}. \tag{3.38}$$

In order to evaluate whether they are suitable independent and conserved quantities of the system, it's useful to write the integrable Hamiltonian (2.2) in terms of the newly found charge operators:

$$\begin{aligned} H = {} & U\left(Q_0 + Q_+ + Q_- - N_4\right)^2 + \nu\left(Q_0 + Q_+ + Q_- - N_4\right) \\ & - \sqrt{3}J\left(a_4^\dagger b_0 + b_0^\dagger a_4\right) - \zeta\left(Q_+ - Q_-\right). \end{aligned} \tag{3.39}$$

By analyzing Equation (3.39), we find that Q_0 does not commute with the Hamiltonian due to the $a_4^\dagger b_0 + b_0^\dagger a_4$ tunneling term, whereas Q_+, Q_- and N yield

$$\begin{aligned} [H, Q_+] = [H, Q_-] = [H, N] = 0, \\ [Q_+, Q_-] = [N, Q_+] = [N, Q_-] = 0, \end{aligned} \tag{3.40}$$

which indicates that Q_+ and Q_- are suitable independent and conserved quantities of the system. Therefore, we may choose

$$\{H, N, Q_+, Q_-\} \tag{3.41}$$

as the set of four algebraically independent conserved operators of the four-site model, establishing integrability [22, 29, 30]. Going back to Equation (3.23), we can see that Q_+ and Q_- can only be conserved quantities when the long-range interaction,

$$\left(U_{12} - U_0\right)\left(N_1 N_2 + N_2 N_3 + N_3 N_1\right), \tag{3.42}$$

is cancelled out, hence the integrability condition $U_{12} = U_0$. This is made evident when one takes the inverse transforms

$$\begin{aligned} N_1 &= \frac{1}{3}\left(b_0^\dagger + b_+^\dagger + b_-^\dagger\right)\left(b_0 + b_+ + b_-\right), \\ N_2 &= \frac{1}{3}\left(b_0^\dagger + \sigma^{-1} b_+^\dagger + \sigma b_-^\dagger\right)\left(b_0 + \sigma b_+ + \sigma^{-1} b_-\right), \\ N_3 &= \frac{1}{3}\left(b_0^\dagger + \sigma b_+^\dagger + \sigma^{-1} b_-^\dagger\right)\left(b_0 + \sigma^{-1} b_+ + \sigma b_-\right), \end{aligned} \tag{3.43}$$

and tries to evaluate the commutation relations between the mixed long-range terms of Equation (3.42) and the charge operators of (3.36).

3.4 Quantum dynamics

In this section, we present the different dynamical regimes of the four-site integrable model at $\Omega = 0$. This is studied through the population expectation values at each site, $\langle N_j \rangle \equiv \langle \Psi(t) | N_j | \Psi(t) \rangle$, where the time evolution of the system is given by

$$|\Psi(t)\rangle = \exp(-itH) |\Psi(0)\rangle, \tag{3.44}$$

in units with $\hbar = 1$. The above states are represented throughout the text in the occupancy basis of the four sites for $N = n_1 + n_2 + n_3 + n_4$ conserved particles:

$$|n_1, n_2, n_3, n_4\rangle = \frac{(a_1^\dagger)^{n_1}}{\sqrt{n_1!}} \frac{(a_2^\dagger)^{n_2}}{\sqrt{n_2!}} \frac{(a_3^\dagger)^{n_3}}{\sqrt{n_3!}} \frac{(a_4^\dagger)^{n_4}}{\sqrt{n_4!}} |0\rangle \tag{3.45}$$

where $|0\rangle \equiv |0, 0, 0, 0\rangle$. In all figures, we assume the system to be in an initial state where all atoms occupy site 1, $|\Psi(0)\rangle = |N, 0, 0, 0\rangle$.

The interaction and external field terms of Hamiltonian (3.30) show that the energy in the system is set by the initial population imbalance between the central site and the three outer sites. This allows us to characterize the dynamical regimes by the dimensionless parameter

$$\chi = \left| \frac{U(N - 2k) + \nu/2}{J} \right|, \tag{3.46}$$

where k is the central site's initial population, which quantifies the current ratio between interaction strength and tunneling amplitude in the system. Following [21, 23, 39, 40], the population dynamics can be split into three distinct interaction regimes, characterized by $\chi \ll 1$ (Rabi), $\chi \sim 1$ (Josephson) and $\chi \gg 1$ (Fock).

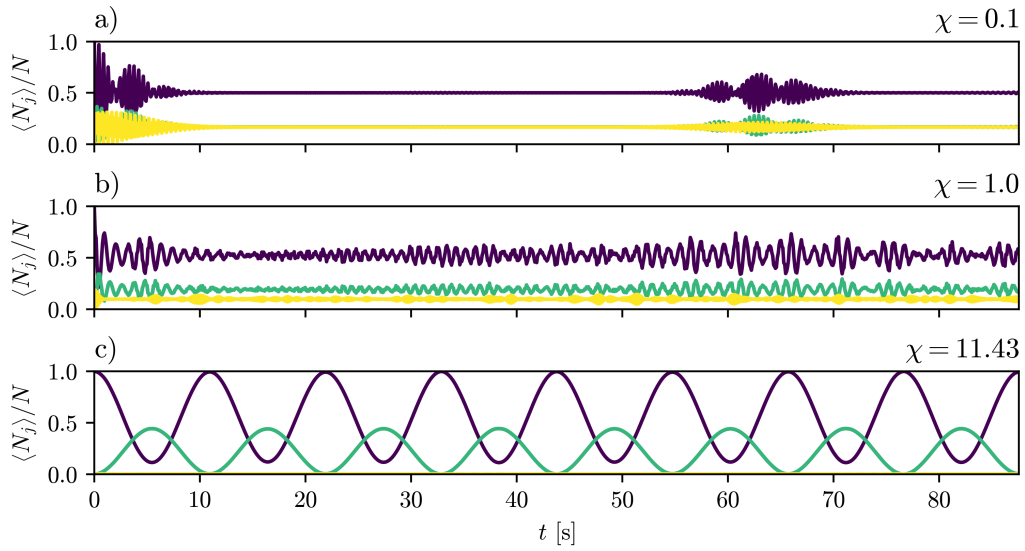

Figure 3.1: Fractional population dynamics at $\Omega = 0$, obtained by the exact numerical diagonalization of (3.30). The time evolution of $\langle N_1 \rangle / N$ (purple), $\langle N_2 \rangle / N$ (blue), $\langle N_3 \rangle / N$ (green) and $\langle N_4 \rangle / N$ (yellow) was obtained for the cases (a) $\chi \ll 1$, (b) $\chi \sim 1$ and (c) $\chi \gg 1$. In all cases, we set $N = 16$, $J/h = 8.22$ Hz and $\nu = U$.

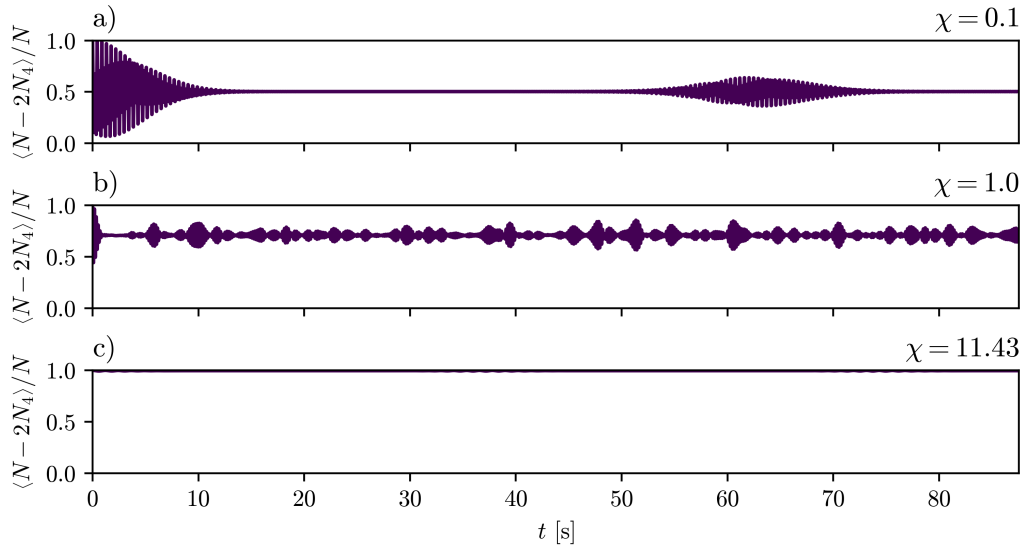

Figure 3.2: Fractional population imbalance between the central site and the three outer sites at $\Omega = 0$. The time evolution of $\langle N - 2N_4 \rangle / N$ (purple) was obtained for the cases (a) $\chi \ll 1$, (b) $\chi \sim 1$ and (c) $\chi \gg 1$. In all cases, we set $N = 16$, $J/h = 8.22$ Hz and $\nu = U$.

Figure 3.1 shows the fractional population dynamics of the system for increasing values of χ. We can see that, as interaction strength increases, tunneling between the central site and the outer site subsystem decreases, eventually vanishing in the strong interaction regime, where all atoms can be found confined to their initial subsystems. This behavior results from two combined effects. First, the interaction terms $U\left(N - 2N_4\right)^2$ and $\nu\left(N - 2N_4\right)$ of Hamiltonian (3.30) introduce a tilt between the central and outer sites that confines the atoms to these subsystems as χ increases. On the other hand, the cancellation of long-range interaction term $\left(U_{12} - U_0\right)\left(N_1N_2 + N_2N_3 + N_3N_1\right)$ due to the integrability condition transforms the outer sites into an effectively noninteracting subsystem, where atoms can tunnel freely via a second-order process through the central site [32]. Furthermore, we can see that the dynamics go from a pattern of collapse and revival of oscillations, similar to acoustic beating, to harmonic oscillations, where the initial imbalance between the central and outer sites is conserved, as seen in Figure 3.2.

Figure 3.2 shows the time evolution of the population imbalance between the central site and outer site subsystem for increasing values of χ, and serves to highlight the self-confinement behavior that emerges in the strong interaction regime. If we consider the central site and the outer site subsystem to form a two-level system, we find the population dynamics between the central site and the outer-site subsystem to be dynamically equivalent to that of the two-site Bose-Hubbard model [21], in which the same pattern of collapse and revival of oscillations of Figure 3.2 (a) and the self-confinement behavior of Figure 3.2 (c) can be found.

Hereby, the text will solely focus on the strong interaction regime, referred to as "resonant tunneling" regime. The conserved charges of the four-site model can be used to write an effective Hamiltonian for the resonant regime. This effective Hamiltonian provides a better lens through which to analyze the resonant regime, and will allow us to derive analytical expressions for the time evolution of the outer site populations in a more convenient manner.

3.5 Effective Hamiltonian

In this section we derive an effective Hamiltonian dynamically equivalent to the system's resonant tunneling regime.

In the resonant regime, tunneling occurs as if the central site and the outer sites were two isolated noninteracting subsystems. As mentioned before, atoms are able to tunnel as if the outer sites were directly connected via a second-order transition through the central site. Due to symmetry, we can expect the effective tunneling potential between neighboring outer sites to be

$$V_{ij} = -J_{\text{eff}} \left(a_i^\dagger a_j + a_j^\dagger a_i \right), \tag{3.47}$$

independent of neighbor choice. Since $\langle N_4 \rangle$ is constant and rotation induced tunneling remains unaffected in the resonant regime, we may write the effective Hamiltonian as:

$$H_{\text{eff}} = -J_{\text{eff}} \left(a_1^\dagger a_2 + a_2^\dagger a_1 + a_2^\dagger a_3 + a_3^\dagger a_2 + a_3^\dagger a_1 + a_1^\dagger a_3 \right) - \zeta \mathcal{J} \tag{3.48}$$

The effective tunneling amplitude J_{eff} can be obtained by calculating the transition rate of the central site second-order process. In the resonant regime, we may treat the tunneling terms of Hamiltonian (3.30) as a weak physical disturbance

$$V = -J \sum_{i=1}^{3} \left(a_i^\dagger a_4 + a_4^\dagger a_i \right) \tag{3.49}$$

such that $H = H_0 + V$, where H_0 are the unperturbed interaction and rotation terms of Hamiltonian (3.30):

$$H_0 = U \left(N - 2N_4 \right)^2 + \nu \left(N - 2N_4 \right) - \zeta \mathcal{J} \tag{3.50}$$

Then, according to perturbation theory, the second-order transition rate can be written as [41]

$$T_{i \to f} = \sum_s \frac{\langle f | V | s \rangle \langle s | V | i \rangle}{E_i^{(0)} - E_s^{(0)}}, \tag{3.51}$$

where $|i\rangle$ and $|f\rangle$ are the initial and final states of the transition and $E_i^{(0)} = \langle i | H_0 | i \rangle$. The sum over s considers all intermediary states $|s\rangle$ that can be connected from $|i\rangle$ to $|f\rangle$ via two consecutive applications of the perturbation V. In this context, we may describe the second-order transition of a particle from site 1 to site 2 with the following orderings:

$$\begin{aligned} &(i) \quad |i\rangle = |n, m, l, k\rangle \to |s_1\rangle = |n-1, m, l, k+1\rangle \to |f\rangle = |n-1, m+1, l, k\rangle \\ &(ii) \quad |i\rangle = |n, m, l, k\rangle \to |s_2\rangle = |n, m+1, l, k-1\rangle \to |f\rangle = |n-1, m+1, l, k\rangle \end{aligned} \tag{3.52}$$

where n, m, l and k are the expected values of N_1, N_2, N_3 and N_4 at $t = 0$, such that $N = n + m + l + k$. Plugging the states of Equation (3.52), V and H_0 into Equation (3.51) yields a transition rate of (see Appendix A.1)

$$T_{i \to f} = \frac{J^2}{4U} \left(\frac{k+1}{N - 2k - 1 + \frac{\nu}{2U}} - \frac{k}{N - 2k + 1 + \frac{\nu}{2U}} \right) \sqrt{n} \sqrt{m+1}. \tag{3.53}$$

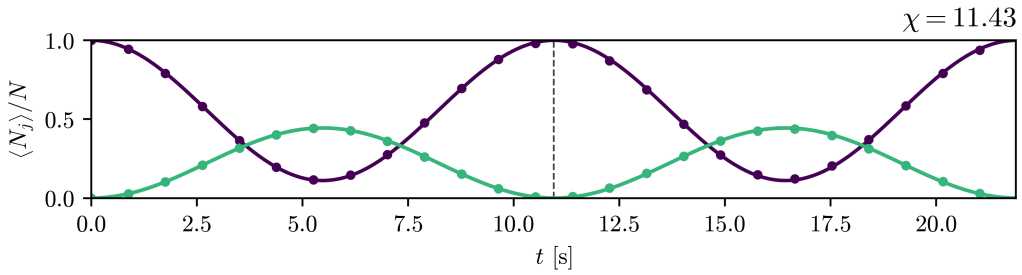

Figure 3.3: Comparison between the analytical results obtained by using (3.57) in the time evolution operator (line) and the dynamics obtained by the numerical diagonalization of (3.30) (dots) for the fractional site populations at $\Omega = 0$. The time evolution of $\langle N_1 \rangle / N$ (purple), $\langle N_2 \rangle / N$ (blue) and $\langle N_3 \rangle / N$ (green) was obtained for $|\Psi(0)\rangle = |N, 0, 0, 0\rangle$, $N = 16$, $J/h = 8.22$ Hz, $\nu = U$ and $\chi = 11.43$ (resonant regime). The vertical line represents $t = 2\pi h/\xi$.

Since the lowest nonzero order of perturbation for the transition of a particle must be equal for both Hamiltonians, we must also have

$$T_{i \to f} = \langle f | H_{\text{eff}} | i \rangle = -J_{\text{eff}} \sqrt{n} \sqrt{m+1}, \tag{3.54}$$

which by comparison leads to

$$J_{\text{eff}} = -\frac{J^2}{4U} \left(\frac{k+1}{N - 2k - 1 + \frac{\nu}{2U}} - \frac{k}{N - 2k + 1 + \frac{\nu}{2U}} \right). \tag{3.55}$$

From here, it's useful to write the effective Hamiltonian in terms of the conserved charges found in Section 3.3. Substituting for Equations (3.36), (3.37) and (3.38) in Equation (3.48) leads to

$$H_{\text{eff}} = -J_{\text{eff}} \left[2 \left(N - 2N_4 \right) + 3 \left(Q_+ + Q_- \right) \right] - \zeta \left(Q_+ - Q_- \right). \tag{3.56}$$

Since $\langle N - 2N_4 \rangle$ is conserved in the resonant regime, we may take a reduced form for the effective Hamiltonian:

$$H_{\text{eff}} = -\left(\xi + \zeta \right) Q_+ - \left(\xi - \zeta \right) Q_- \tag{3.57}$$

where we define the effective tunneling amplitude

$$\xi = \frac{3J^2}{4U} \left(\frac{k+1}{N - 2k - 1 + \frac{\nu}{2U}} - \frac{k}{N - 2k + 1 + \frac{\nu}{2U}} \right). \tag{3.58}$$

Figure 3.3 shows a comparison between the dynamics obtained by the numerical diagonalization of Hamiltonian (3.30) and the analytical results obtained by using the effective Hamiltonian (3.57) in the time evolution operator. The perfect match between the results confirms the effective Hamiltonian is dynamically equivalent to the resonant regime. The analytical expressions for the expectation values of the site populations and the time evolution of the system obtained through the effective Hamiltonian are presented in the next chapter, where we discuss the effects of rotation in the dynamics of the resonant regime.

Chapter 4

Quantum rotation sensor

This chapter details the application of the four-site integrable model as a quantum rotation sensor. We start with an overview of quantum metrology and sensitivity scaling and later propose and discuss a rotation sensing protocol for the system.

4.1 Quantum metrology

The goal of metrology is to estimate the value of a parameter whilst achieving the lowest possible measurement uncertainty in the process. This is done by identifying a suitable probe system sensitive to changes in a given parameter of interest and then designing a measurement scheme around it optimized for precision. In this context, we can expect measurement uncertainty to depend on the initial state of the probe, its evolution, and the readout measurement made to extract information about the parameter.

The number N of elementary units that form a probe (e.g photons in an interferometer or particles in a many-body system) is the most important resource put into any measurement. Because of that, the performance of a measurement scheme is often evaluated by how it scales with N. Classical and semi-classical schemes are limited by the so-called quantum-noise or shot-noise limit, where uncertainty scales with $1/\sqrt{N}$. Quantum-enhanced measurement schemes exploit non-classical resources like quantum entanglement and squeezing to improve sensitivity, and are limited by the so-called Heisenberg limit, where uncertainty scales with $1/N$.

Heisenberg-limited scaling arises from Mandelstam-Tamm type uncertainty relations like [42]

$$\delta\gamma\Delta K_\gamma(t) \geq \frac{1}{2}, \tag{4.1}$$

in units with $\hbar = 1$, where the uncertainty $\delta\gamma$ in a parameter γ, which in part determines the state of a quantum system, is related to the standard deviation ΔK_γ of the operator K_γ that translates the state along γ [43]. In the context of metrology, γ is a parameter of interest that appears as a coupling constant in the Hamiltonian of the probe system, and the operator K_γ is the Hermitian generator of displacements in γ defined as [44]

$$K_\gamma(t) = i\frac{\partial U_\gamma(t)}{\partial\gamma}U_\gamma^\dagger(t), \tag{4.2}$$

where $U_\gamma(t)$ is the unitary transform that evolves the probe during the measurement protocol.

The optimal measurement uncertainty for a quantum-enhanced measurement scheme is quantified by the quantum Cramér-Rao bound:

$$(\delta\gamma)^2 \geq \frac{1}{\mathfrak{I}_\gamma(t)}, \tag{4.3}$$

where $\mathfrak{I}_\gamma(t)$ denotes the quantum Fisher information. Given a probe state $\rho_\gamma(t)$, one can think of the classical Fisher information as the amount of the information an observable measured on $\rho_\gamma(t)$ can provide about γ, and quantum Fisher information as a measure of the information $\rho_\gamma(t)$ as a whole can provide about γ. Therefore, quantum Fisher information can be defined as the maximization of classical Fisher information over all possible measurements of $\rho_\gamma(t)$ [45, 46]. Following [44–48], it can be shown that, if the probe state is pure ($\rho_\gamma^2 = \rho_\gamma$) and K_γ is a Hermitian operator, the quantum Fisher information becomes

$$\mathfrak{I}_\gamma(t) = 4\Delta^2 K_\gamma(t) \tag{4.4}$$

where $\Delta^2 K_\gamma$ denotes the variance of K_γ, thus recovering the Mandelstam-Tamm type uncertainty relation described in (4.1):

$$\delta\gamma \geq \frac{1}{2\Delta K_\gamma(t)}. \tag{4.5}$$

In quantum metrology, the probe's Hamiltonian is often linearly coupled to the parameter of interest γ. This is referred to as linear (quantum) metrology. The general linear metrology Hamiltonian can be written as

$$H_\gamma = \gamma h_0 = \gamma \sum_{j=1}^{N} h_j \tag{4.6}$$

where h_j is the coupling Hamiltonian of the j-th probe unit. The generator of translations in γ for Hamiltonian (4.6), considering the system to evolve under the time evolution operator, is

$$K_\gamma(t) = i\frac{\partial}{\partial\gamma}\left(e^{-it\gamma h_0}\right)e^{it\gamma h_0} = th_0. \tag{4.7}$$

If the probe units are prepared in separable states, i.e., no quantum resources are used, the spread in K_γ is simply $\Delta K_\gamma = t\sqrt{N}\Delta h_j$. The best possible uncertainty in this scenario is set by the maximum of Δh_j, which is bounded by $\Delta h_j \leq (\Lambda - \lambda)/2$, where Λ and λ are the largest and smallest eigenvalues of h_j [49]. This, through Equation (4.5), leads to the classical shot-noise sensitivity scaling:

$$\delta\gamma \geq \frac{1}{t\sqrt{N}(\Lambda - \lambda)}. \tag{4.8}$$

On the other hand, if the probe units can be entangled, the best possible uncertainty is set by the maximum of Δh_0 in $\Delta K_\gamma = t\Delta h_0$, which for N identical probe units is bounded by $\Delta h_0 \leq (N\Lambda - N\lambda)/2$, where $N\Lambda$ and $N\lambda$ are the largest and smallest eigenvalues of h_0 [43, 49]. This leads to the previously mentioned Heisenberg limit of quantum metrology:

$$\delta\gamma \geq \frac{1}{tN(\Lambda - \lambda)}. \tag{4.9}$$

The optimal bounds set by (4.9) and (4.8) can be attained by employing probe states that maximize the spread in K_γ and an appropriate readout measurement that minimizes uncertainty. For separable probe states, the optimal states correspond to the equally weighed superpositions

$$|\Psi_j(0)\rangle = \frac{1}{\sqrt{2}}\left(|\Lambda_j\rangle + |\lambda_j\rangle\right), \tag{4.10}$$

where $|\Lambda_j\rangle$ and $|\lambda_j\rangle$ denote the eigenstates corresponding to the largest and smallest eigenvalues of the j-th probe unit. For the case where entanglement can be used, the optimal states correspond to a special class of "all-or-nothing" entangled superpositions called NOON states:

$$|\Psi(0)\rangle = \frac{1}{\sqrt{2}}\left(|\Lambda_1 \ldots \Lambda_N\rangle + |\lambda_1 \ldots \lambda_N\rangle\right). \tag{4.11}$$

In both cases, the optimal readout can be performed by measuring the observable $\sigma_{x;j} = |\lambda_j\rangle\langle\Lambda_j| + |\Lambda_j\rangle\langle\lambda_j|$ separately on each probe unit [49].

In order to provide an example of what we have discussed so far, let's consider the task of estimating the phase $\varphi \equiv \gamma t$ introduced by time evolution in an ensemble of two-level systems, where $\Lambda = 1$ and $\lambda = 0$ are the two levels. We start by considering a typical interferometry protocol where the systems evolve independently and are prepared in identical initial states. The protocol begins by initializing all of the systems in superpositions given by

$$|\Psi_j(0)\rangle = \frac{1}{\sqrt{2}}\left(|0_j\rangle + |1_j\rangle\right), \tag{4.12}$$

which are then let to evolve under $U_\gamma(t) = \exp(itH_\gamma)$ for a time t. This introduces a relative phase between the superposition components, changing them to

$$|\Psi_j(t)\rangle = \frac{1}{\sqrt{2}}\left(|0_j\rangle + e^{i\gamma t}|1_j\rangle\right). \tag{4.13}$$

The final readout is performed by measuring the observable $\sigma_{x;j} = |0_j\rangle\langle 1_j| + |1_j\rangle\langle 0_j|$ separately on each system, resulting in a measured signal of [50]

$$\langle\sigma_x\rangle \equiv \sum_{j=1}^{N}\langle\sigma_{x;j}\rangle = \sum_{j=1}^{N}\langle\Psi_j(t)|\,\sigma_{x;j}\,|\Psi_j(t)\rangle = N\cos(\gamma t) \tag{4.14}$$

with variance

$$\Delta^2\sigma_x \equiv \sum_{j=1}^{N}\left(\langle\sigma_{x;j}^2\rangle - \langle\sigma_{x;j}\rangle^2\right) = N\sin^2(\gamma t). \tag{4.15}$$

The uncertainty in the estimate of γ from the measurement in Equation (4.14) can be obtained through error propagation as [47]

$$\delta\gamma = \frac{\Delta\sigma_x}{|\partial_\gamma\langle\sigma_x\rangle|} = \frac{1}{t\sqrt{N}}, \tag{4.16}$$

which corresponds to the classical optimal uncertainty set by Equation (4.8).

As previously alluded to, the protocol is unable to achieve Heisenberg scaling due to the use of separable states. The reason this happens is quite simple: since the two-level systems are independent, measuring them one at a time or all at once yields the same result. In both cases, the final readout is an average over all $\sigma_{x;j}$ measurements, which for large N will always result in an error scaling of $1/\sqrt{N}$ due to the central limit theorem [49].

This issue can be circumvented by employing entanglement at the probe preparation stage. If the ensemble is initialized in a NOON state the likes of (4.11),

$$|\Psi(0)\rangle = \frac{1}{\sqrt{2}}\left(|0_1 \dots 0_N\rangle + |1_1 \dots 1_N\rangle\right), \tag{4.17}$$

evolution under $U_\gamma(t)$ introduces a global phase that accumulates N times faster than in the separable states of (4.13):

$$|\Psi(t)\rangle = \frac{1}{\sqrt{2}}\left(|0_1 \dots 0_N\rangle + e^{iN\gamma t}|1_1 \dots 1_N\rangle\right) \tag{4.18}$$

The final readout can still be performed via separable measurements of $\sigma_{x;j}$, yielding

$$\langle\sigma_x\rangle \equiv \langle\Psi(t)|\bigoplus_{j=1}^{N}\sigma_{x;j}|\Psi(t)\rangle = \cos(N\gamma t) \text{ and } \Delta^2\sigma_x = \sin^2(N\gamma t). \tag{4.19}$$

If we now calculate the uncertainty in the estimate of γ, we get the optimal quantum metrology uncertainty scaling set by Equation (4.9):

$$\delta\gamma = \frac{\Delta\sigma_x}{|\partial_\gamma\langle\sigma_x\rangle|} = \frac{1}{tN} \tag{4.20}$$

which corresponds to a sensitivity improvement of $1/\sqrt{N}$ over the use of separable states. Interestingly enough, entanglement turns out to be useless in the readout stage, as swapping the final readout for an entangled observable like

$$\sigma_x = |0_1 \dots 0_N\rangle\langle 1_1 \dots 1_N| + |1_1 \dots 1_N\rangle\langle 0_1 \dots 0_N| \tag{4.21}$$

amounts to no improvement in sensitivity [49]. From the steps leading to (4.20), it becomes clear that the observed sensitivity improvement is a direct consequence of the entangled state of Equation (4.13) evolving N times faster than the separable states of Equation (4.18).

The key takeaway from the examples described here is that the appropriate use of entanglement at the probe preparation stage of a protocol can improve its sensitivity by a factor of $1/\sqrt{N}$ over the use of separable states, due to entangled states evolving faster than separable configurations of the same physical resources [49]. This is a purely quantum effect that many quantum metrology protocols take advantage of to achieve Heisenberg scaling [24, 51, 52]. Moreover, since entanglement is not always a viable option in practical settings, the use of separable states can be seen as an active $1/\sqrt{N}$ cost to measurement precision.

Regardless, it's always desirable to have alternative means of improving uncertainty scaling. With nonlinear interactions [26, 43, 53–56] or time-dependant evolutions and error correction schemes [57–62], for example, it's possible to achieve local precisions that scale beyond the Heisenberg limit, even when entanglement is not used. In the next sections, we argue, based on the application of the four-site integrable model as a rotation sensor, that second-order processes may offer another avenue to improve uncertainty scaling in the absence of entanglement.

4.2 Quantum dynamics under rotation

In this section, we analyze the influence of rotation on the dynamics of the system in the resonant regime. This is studied through the expectation values $\langle N_j \rangle$, following Section 3.4.

In order to minimize initial state engineering, we assume the initial state of the system to be

$$|\Psi(0)\rangle = |N,0,0,0\rangle = \frac{(a_1^\dagger)^N}{\sqrt{N!}}|0\rangle \tag{4.22}$$

where all atoms occupy site 1. Using the effective Hamiltonian (3.57) in the time evolution operator (3.44), it is observed that the above state evolves into a coherent state in the resonant regime (see Appendix A.2):

$$|\Psi(t)\rangle = \frac{\left[\sigma_1(t)\, a_1^\dagger + \sigma_2(t)\, a_2^\dagger + \sigma_3(t)\, a_3^\dagger\right]^N}{3^N\sqrt{N!}}|0\rangle \tag{4.23}$$

where $\sigma_j(t) = 1 + 2e^{-it\xi}\cos\theta_j(t)$ and $\theta_j(t) = t\zeta + 2\pi(j-1)/3$ for $j = 1,2,3$. This leads to an analytical expression for the expectation values of the outer site populations, given by (see Appendix A.3):

$$\langle N_j \rangle = \frac{N}{9}\left(1 + 4\cos\theta_j(t)\left[\cos(t\xi) + \cos\theta_j(t)\right]\right). \tag{4.24}$$

By analyzing Equation (4.24), we can identify the period of the harmonic dynamics observed in the resonant regime to be $T = 2\tau$, where $\tau \equiv \pi/\xi$.

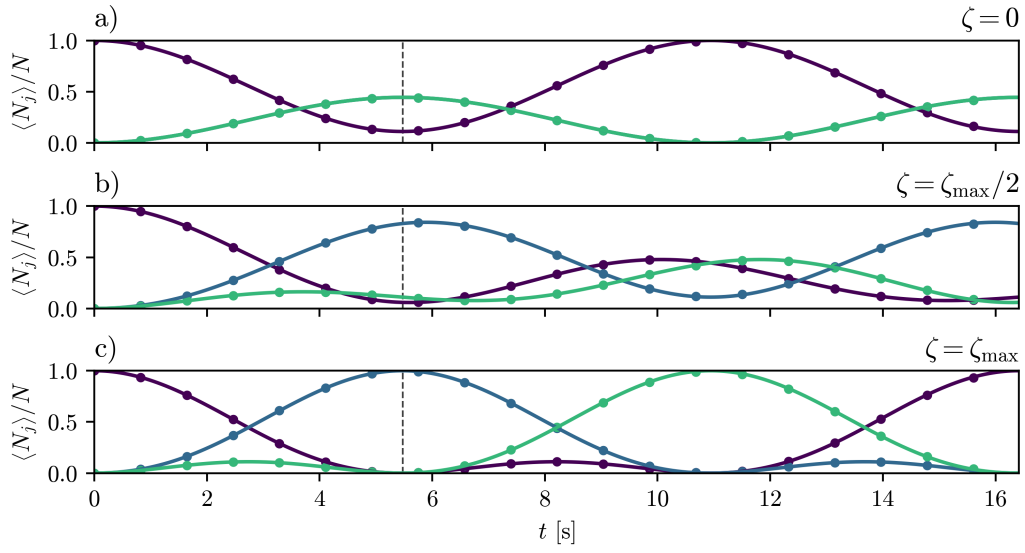

Figure 4.1: Comparison between the analytical results of (4.24) (line) and the numerical diagonalization of (3.30) (dots) for the fractional site populations. The time evolution of $\langle N_1 \rangle / N$ (purple), $\langle N_2 \rangle / N$ (blue), $\langle N_3 \rangle / N$ (green) was obtained for the cases (a) $\zeta = 0$, (b) $\zeta = \zeta_{\max}/2$ and (c) $\zeta = \zeta_{\max}$, where $\zeta_{\max} \equiv \xi/3$. In all cases, we set $N = 16$, $J/h = 8.22$ Hz, $\nu = U$ and $\chi = 11.43$ (resonant regime). The vertical line represents $t = \pi h/\xi$.

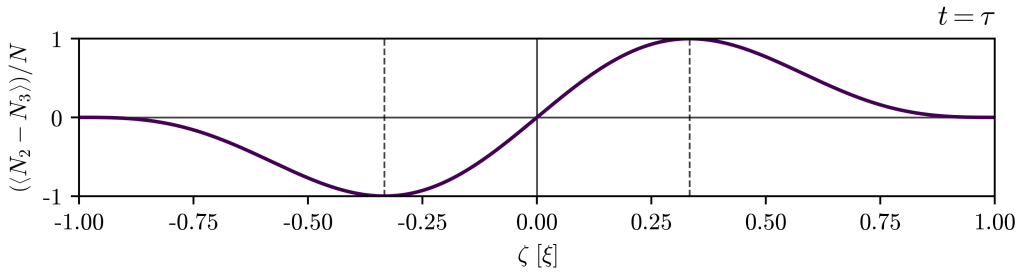

Figure 4.2: Analytical results of (4.25) for the fractional population imbalance between sites 2 and 3 as a function of ζ. The vertical dashed lines represent $\zeta = \pm\zeta_{\max}$.

Figure 4.1 shows the fractional population dynamics of sites 1, 2 and 3 for increasing values of ζ. In the absence of rotation, as seen in Figure 4.1 (a), the initial population in site 1 is evenly transferred between sites 2 and 3 after the time interval $t = \tau$. Figures 4.1 (b) and (c), on the other hand, show that this transfer becomes progressively more unbalanced towards site 2 as rotation increases, reaching maximum imbalance at $\zeta = \zeta_{\max} \equiv \xi/3$, as seen in Figure 4.1 (c). This indicates tunneling ratios are being skewed towards the direction of rotation as rotation speed increases, which is reflective of the opposite clockwise and counterclockwise tunneling structures of Q_- and Q_+ in the effective Hamiltonian (3.57), where increasing ζ sets a clear imbalance in favor of Q_+. This behavior is in accordance with Equation (3.27), where rotation is seen to introduce effective tunneling amplitudes to the system's Hamiltonian, hence the skewed tunneling.

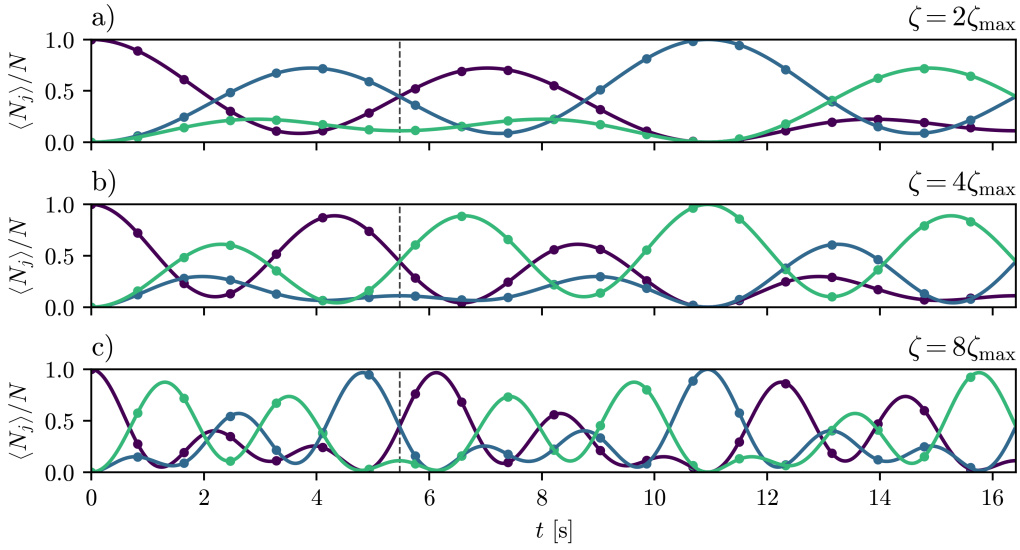

Figure 4.3: Comparison between the analytical results of (4.24) (line) and the numerical diagonalization of (3.30) (dots) for the fractional site populations. The time evolution of $\langle N_1 \rangle / N$ (purple), $\langle N_2 \rangle / N$ (blue), $\langle N_3 \rangle / N$ (green) was obtained for the cases (a) $\zeta = 2\zeta_{\max}$, (b) $\zeta = 4\zeta_{\max}$ and (c) $\zeta = 8\zeta_{\max}$, where $\zeta_{\max} \equiv \xi/3$. In all cases, we set $N = 16$, $J/h = 8.22$ Hz, $\nu = U$ and $\chi = 11.43$ (resonant regime). The vertical line represents $t = \pi h/\xi$.

Figure 4.1 makes it clear that there is a one-to-one correspondence between angular velocity and the population imbalance of sites 2 and 3 at $t = \tau$. By analyzing the formula for the imbalance, obtained through Equation (4.24) as

$$\langle N_2 - N_3 \rangle|_{t=\tau} = \frac{2N}{3\sqrt{3}} \left[\sin\left(2\pi\zeta/\xi\right) + 2\sin\left(\pi\zeta/\xi\right) \right], \tag{4.25}$$

we find that the rotation-to-imbalance correspondence at $t = \tau$ is only valid in the interval $|\zeta| \leq \xi/3$, since Equation (4.25) stops being monotonic outside this interval, as seen in Figure 4.2. Hence, the definition of $\zeta_{\max} \equiv \xi/3$ earlier. Indeed, Figure 4.3 shows that it becomes impossible to correlate rotation to population imbalance for $|\zeta| > \zeta_{\max}$, as the dynamics start to display clear signs of beating due to site populations naturally oscillating over time in the absence of rotation.

4.3 Optimal rotation sensing bounds

From the analysis in the previous section, we find that at $t = \tau$ there is a one-to-one correspondence in the interval $|\zeta| \leq \zeta_{\max}$, where increasing angular velocity directly increases population imbalance. This feature underpins the four-site integrable model as a suitable platform for rotation sensing, since it allows us to estimate rotation through site population measurements. Thus, to better understand the system from the perspective of rotation sensing, it's helpful to derive its optimal rotation sensing bounds.

Following the quantum metrology concepts presented in Section 4.1, the generator of translations in Ω, our parameter of interest, for Hamiltonian (3.30) is

$$K_\Omega(t) = i\frac{\partial}{\partial\Omega}\left(e^{-itH}\right)e^{itH} = tW\mathcal{J} \tag{4.26}$$

where $\mathcal{J}$ is the current operator given by (3.31) and W is the angular quasimomentum defined in (3.29), which combined provide the second quantization of angular momentum in the four-site occupancy basis (3.45):

$$\boldsymbol{\Omega} \cdot \hat{\boldsymbol{L}}(\boldsymbol{r}) = \Omega W \mathcal{J}. \tag{4.27}$$

By comparison with Equation (4.7), the optimal uncertainty for $K_\Omega(t)$ is set by the largest and smallest single-particle eigenvalues of $\mathcal{J}$, $\Lambda = +1$ and $\lambda = -1$, corresponding to the counterclockwise and clockwise modes of circulation of the system given by Equation (3.33). Thus, according to Equation (4.9), the four-site integrable model, as expected, is inherently Heisenberg limited:

$$\delta\Omega \geq \frac{1}{2tWN}. \tag{4.28}$$

Since the rotation-to-imbalance correspondence we wish to exploit requires measurements to be taken at $t = \tau$, we observe from Equation (3.58) that at $t = \tau = \pi/\xi$ we have (note that Equation (4.28) assumes all particles in the system are being used for rotation sensing, i.e., $k = 0$)

$$\delta\Omega \geq \frac{1}{2\tau WN} = \frac{3J^2}{8\pi WUN\left(N - 1 + \frac{\nu}{2U}\right)} \propto \frac{1}{N^2}, \tag{4.29}$$

which corresponds to an improvement of $1/N$ over the Heisenberg limit due to the additional dependence of τ on N. Following the steps that lead to the definition of ξ in Section 3.5, we can see that this additional scaling comes from the $1/N$ dependence found in the second-order transition rates obtained through Equation (3.51), which is a direct consequence of the quadratic coupling between interaction energy and particle number found in the system, given by $U\left(N-2N_4\right)^2$. Indeed, if this coupling was linear instead of quadratic, we would have $E_i^{(0)}-E_s^{(0)}\sim 2U$, leading to no scaling advantage. Note that this implies that the advantage is also lost when $\nu \gg UN$, due to the external field overpowering the nonlinear interactions of the system; hence, the rightmost side of (4.33) is only valid for $\nu \lesssim UN$.

As discussed in Section 4.1, the optimal bound set by Equation (4.29) can be theoretically achieved by employing a NOON state of the form

$$|\Psi(0)\rangle = \frac{1}{\sqrt{2}}\left(|0,N,0\rangle + |0,0,N\rangle\right) = \frac{(b_+^\dagger)^N + (b_-^\dagger)^N}{\sqrt{2}\sqrt{N!}}|0\rangle \tag{4.30}$$

and measuring the observable $\sigma_x \equiv |0,N,0\rangle\langle 0,0,N| + |0,0,N\rangle\langle 0,N,0|$, where $|0,N,0\rangle$ and $|0,0,N\rangle$ are the eigenstates given by Equation (3.35) corresponding to the largest and smallest eigenvalues of $\mathcal{J}$. Whether σ_x is a real, measurable observable and how one would go about engineering a NOON state the likes of (4.30) are left as open challenges for future investigation.

Assuming σ_x can be measured but the NOON state of Equation (4.30) is not feasible, the second best bound for rotation sensing at $t=\tau$, according to (4.8), would be

$$\delta\Omega \geq \frac{1}{2\tau W\sqrt{N}} = \frac{3J^2}{8\pi WU\sqrt{N}\left(N-1+\frac{\nu}{2U}\right)} \propto \frac{1}{N^{3/2}} \tag{4.31}$$

which is still a factor of $1/\sqrt{N}$ better than the Heisenberg limit. Interestingly, this bound is not actually achievable in the four-site integrable model, since its limited Hilbert space makes it impossible to produce the separable states of Equation (4.10). We can get remarkably close to it, however, as we will discuss in the next section.

4.4 Rotation sensing protocol

Provided the system's parameters are appropriately tuned to achieve the resonant regime and measured rotation speeds are within $|\zeta| \leq \zeta_{\max}$, a rotation sensing protocol using the four-site integrable model can be performed as follows (see Figure 4.4):

(i) Initialize the system in a state where all atoms occupy one of the three outer sites;

(ii) Let the system evolve for a time $t=\tau$;

(iii) At $t=\tau$, measure the population imbalance between the two initially unoccupied sites.

After these steps, the population imbalance measured in step (iii) can be used to estimate $\Omega = \zeta/W$ through Equation (4.25).

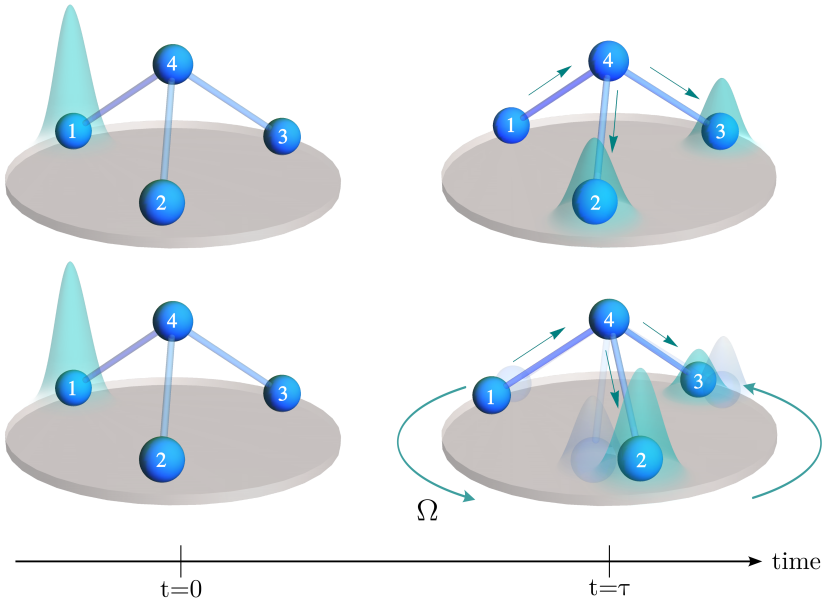

Figure 4.4: Schematic figure of the rotation sensing protocol. The system is prepared in an initial state where all atoms occupy site 1 and evolves for a time τ. For $\Omega = 0$ (top), the initial population is equally transferred between sites 2 and 3. For $\Omega > 0$ (bottom), tunneling becomes biased towards the direction of rotation, setting an imbalance between sites 2 and 3 which can be measured to estimate angular velocity. The straight arrows represent tunneling directions. The circulating arrow represents $\boldsymbol{\Omega} = \Omega\hat{z}$.

Following section 4.1, the uncertainty in the estimate of Ω can be obtained through error propagation as (see Appendix A.4)

$$\delta\Omega = \frac{\Delta\left(N_2 - N_3\right)}{\left|\partial_\Omega \left\langle N_2 - N_3 \right\rangle\right|} = \frac{f\left(\zeta\right)}{2\tau W\sqrt{2N}}, \tag{4.32}$$

where $f\left(\zeta\right) \sim \sqrt{3}$ is a smooth and convex curve that has little variation in the interval $|\zeta| \leq \zeta_{\max}$. Since step (i) assumes the central site is initially empty, we observe from Equation (3.58) that, since $\tau = \pi/\xi$, we have

$$\delta\Omega \geq \frac{3J^2 f\left(\zeta\right)}{8\pi UW\sqrt{2N}\left(N - 1 + \frac{\nu}{2U}\right)} \propto \frac{1}{N^{3/2}}. \tag{4.33}$$

which is just a factor of $\sim \sqrt{3/2}$ larger than the optimal sensitivity bound set by Equation (4.31).

As discussed in the previous section, the observed scaling advantage provided by the additional dependence of τ on N results from a nontrivial manifestation of the system's nonlinearity. To compare this result to another cold atom system with "super-Heisenberg" scaling found in the literature, we refer to the nonlinear interferometry scheme provided by Boixo et al. in [43]. They consider a two-mode Bose-Einstein condensate, where the parameters of interest γ_1 and γ_2 that characterize the interaction of the two-modes display quadratic couplings $\gamma_1(a_1^\dagger a_1 + a_2^\dagger a_2 - 1)(a_1^\dagger a_1 - a_2^\dagger a_2)$ and $\gamma_2(a_1^\dagger a_1 - a_2^\dagger a_2)^2$ to the creation and annihilation operators of each mode, yielding an uncertainty that scales with $1/N^{3/2}$ for the estimates of

γ_1 and γ_2. This corresponds to an improvement of $1/\sqrt{N}$ over the Heisenberg limit and is shown to be a direct consequence of the nonlinear nature of the system's many-body interactions. Here, by comparison, the rotation sensing protocol is able to produce estimates of Ω with the same $1/N^{3/2}$ sensitivity despite it being linearly coupled to the creation and annihilation operators of the outer sites, $\sim \Omega(a_1^\dagger a_2 + a_2^\dagger a_3 + a_3^\dagger a_1 - a_2^\dagger a_1 - a_1^\dagger a_3 - a_3^\dagger a_2)$, due to the additional physical resource scaling introduced by nonlinearity to the optimal protocol running time. This indicates that the scaling advantage provided by nonlinearity arises from distinct mechanisms in each case, which points to second-order processes as a possibly unexplored avenue for increasing precision in nonlinear interferometry.

Naturally, there has been some debate about whether these results constitute true violations of the Heisenberg limit. In [54], it's demonstrated that characterizing the resource count of a parameter estimation task in terms of its "query complexity" instead of the number of physical resources it employs solves this paradox, including in the case of [43]. On the other hand, in [63], it's pointed out that a number of authors that suggest nonlinearity provides a scaling advantage do so based on local precision calculations rather than the average estimation error of their schemes, putting into question whether the suggested scaling advantage is real. Since the enhanced precision of the rotation sensing protocol results from a nontrivial mechanism particular to the four-site integrable model, whether its scaling advantage is remains an open question. Of course, since it results from protocol times also scaling with the number of particles, there is a limit to the amount of physical resources one can employ before measurements take an unreasonably long time to be performed, which could offset the scaling advantage.

Nonetheless, the measurement protocol has the advantage of being relatively straightforward compared to other cold atom sensors found in the literature [64–70]. The initial state in step (i) can be obtained by trapping all atoms in a single site, requiring no further state engineering, and the measurement in step (iii) can be performed by measuring the atomic populations at each site, which can be achieved by a myriad of well known procedures [71–73]. These features, regardless of the scaling advantage, underpin the model as another experimentally promising proof-of-principle of cold-atom interferometry. Thus, from here, next steps include further investigation into its physical and experimental realization, which were out of scope for this dissertation.

Chapter 5

Conclusion

In this work we have presented and studied a particular cold atom system described by a four-site integrable model consisting of an ensemble of ultracold dipolar bosons trapped in a rotating, tetrahedral site arrangement. While Chapter 2 served as a general introduction to this dissertation, Chapters 3 and 4 provided a full exploration of the investigated system and its application as a quantum device.

In Chapter 3, we derived the extended Bose-Hubbard model (EBHM) for an ensemble of polarized ultracold magnetic atoms, for a fixed number of particles and isotropic tunnelings. The four-site model was then obtained by restricting the EBHM to the four-site geometry, realized by confining a cubic optical lattice with a harmonic potential. By transforming the model from its stationary frame to a rotating frame, we demonstrated that rotation has the effect of inducing tunneling in the system in a manner akin to the Sagnac effect. This process introduces a current operator to the four-site Hamiltonian, whose exact diagonalization revealed two additional independent and conserved quantities of the system, Q_+ and Q_-, which were shown to be the occupation numbers of the two nonzero modes of circulation found in the system, commuting with both H and N and among themselves. This allowed us to choose $\{H, N, Q_+, Q_-\}$ as the complete set of independent and conserved quantities of the system, establishing integrability.

We then studied the quantum dynamics of the system in the absence of rotation. By treating the central site and the outer sites as separate subsystems, it was observed that the system exhibits a self-confinement behavior whose population dynamics are dynamically equivalent to those of a two-site integrable model. This behavior results from the interaction driven tilts found in the Hamiltonian and the absence of long-range interaction between the outer sites, which allows atoms to tunnel freely via second-order processes through the central site. This was observed to produce an orderly dynamics in the so-called "resonant tunneling" regime, where the outer site populations exhibit harmonic oscillations while $\langle N_1 + N_2 + N_3 \rangle$ and $\langle N_4 \rangle$ remain constant over time. By treating nearest-neighbor tunneling as a weak physical disturbance and calculating the effective tunneling amplitude of the central site second-order processes, we derived an effective Hamiltonian expressed in terms of Q_+ and Q_-, which proved to be helpful in the development of analytical formulae in the resonant regime.

In Chapter 4, we provided a generalist review of linear quantum metrology, going over a useful framework for single parameter estimation using quantum systems as probes. We derived the two optimal uncertainty limits of quantum metrology, the

shot-noise and Heisenberg limits, and presented two general measurement schemes capable of achieving them. By doing so, it was demonstrated that entanglement can improve sensitivity up to factor of $1/\sqrt{N}$ over the use of separable states, due to some entangled states evolving faster than separable configurations using the same physical resources. These results, far from new, were presented for the purposes of providing a short and sweet but comprehensive introduction to linear quantum metrology for those not acquainted with its core concepts.

After this digression, we studied the quantum dynamics of the resonant regime under rotation. By employing the effective Hamiltonian in the time evolution operator, we were able to derive analytical expressions for the time evolution of the outer site populations, which allowed us to plot the dynamics for increasing values of rotation. For an initial state where all atoms occupy site 1, it was observed that, in the absence of rotation, atoms are evenly transferred between sites 2 and 3 after a time $t = \tau$, becoming progressively more unbalanced towards site 2 as rotation increases, reaching a maximum imbalance at $\zeta = \zeta_{\max}$. This allowed us to identify a one-to-one correspondence between angular velocity and population imbalance, which was exploited to design a rotation sensing protocol.

We demonstrated that, provided the system is appropriately tuned to achieve the resonant regime and measured rotations are within $|\zeta| \leq \zeta_{\max}$, one may leverage the resonant regime to estimate rotation through site population measurements. This can be done by initializing the system in a state where all atoms occupy one of the outer sites and then measuring the population imbalance between the two initially unoccupied sites at $t = \tau$. Remarkably, it was observed that the proposed protocol has a sensitivity scaling advantage due to a nontrivial manifestation of the system's nonlinearity, achieving an uncertainty scaling of $1/N^{3/2}$. This result was shown to be inherently enabled by integrability.

The four-site integrable model explored in this dissertation is part of a larger family of multi-site integrable models for ultracold dipolar bosons. So far, these models have shown great potential for modelling atomtronic quantum devices, but have not been thoroughly studied in the context of rotating frames. Thus, we expect the discussions provided in this dissertation to serve as a solid basis to help further develop this unexplored area. Furthermore, by presenting a generalist overview of quantum metrology and applying its concepts to discuss the application of the model as a quantum sensor, we provided a unified blueprint for treating integrable models in the context of metrology. We believe this will help to better guide the study of integrable models and their applications as quantum sensors. Finally, by presenting a cold atom sensor enhanced by integrability, this work also serves to highlight this elegant property and the advantages it provides in the study of ultracold atoms.

Appendix A

Analytical formulae

In this appendix, we provide step-by-step calculations for some of the relevant analytical formulae found throughout the text.

A.1 Second-order transition rates

In this section, we explicitly calculate the transition amplitudes that lead to the second-order transition rate found in Equation (3.53). The transition of a particle from site 1 to site 2 is described by the following orderings:

$$\begin{aligned} &(i) \quad |i\rangle = |n,m,l,k\rangle \to |s_1\rangle = |n-1,m,l,k+1\rangle \to |f\rangle = |n-1,m+1,l,k\rangle \\ &(ii) \quad |i\rangle = |n,m,l,k\rangle \to |s_2\rangle = |n,m+1,l,k-1\rangle \to |f\rangle = |n-1,m+1,l,k\rangle \end{aligned} \tag{A.1}$$

where $N = n+m+l+k$. Starting with $|s_1\rangle$, from Equations (3.49) and (3.50), we have:

$$\begin{aligned} \langle s_1| V |i\rangle &= J\sqrt{k+1}\sqrt{n}, \\ \langle f| V |s_1\rangle &= J\sqrt{k+1}\sqrt{m+1} \end{aligned} \tag{A.2}$$

and

$$\begin{aligned} E_i^{(0)} &= \langle i| H_0 |i\rangle = U\left(N-2k\right)^2 + \nu\left(N-2k\right), \\ E_{s_1}^{(0)} &= \langle s_1| H_0 |s_1\rangle = U\left[N-2\left(k+1\right)\right]^2 - \nu\left[N-2\left(k+1\right)\right], \end{aligned} \tag{A.3}$$

such that

$$\begin{aligned} E_i^{(0)} - E_{s_1}^{(0)} &= U\left\{\left(N-2k\right)^2 - \left[N-2\left(k+1\right)\right]^2\right\} + 2\nu \\ &= 4U\left(N-2k-1+\frac{\nu}{2U}\right). \end{aligned} \tag{A.4}$$

Repeating the same calculations for $|s_2\rangle$ yields

$$\begin{aligned} \langle s_2| V |i\rangle &= J\sqrt{k}\sqrt{n}, \\ \langle f| V |s_1\rangle &= J\sqrt{k}\sqrt{m+1} \end{aligned} \tag{A.5}$$

and

$$\begin{aligned} E_i^{(0)} - E_{s_2}^{(0)} &= U\left\{\left(N-2k\right)^2 - \left[N-2\left(k-1\right)\right]^2\right\} - 2\nu \\ &= -4U\left(N-2k+1+\frac{\nu}{2U}\right). \end{aligned} \tag{A.6}$$

Substituting for Equations (A.2), (A.4), (A.5) and (A.5) in Equation (3.51) leads to Equation (3.53):

$$\begin{aligned} T_{i\to f} &= \sum_s \frac{\langle f|\, V\,|s\rangle\,\langle s|\, V\,|i\rangle}{E_i^{(0)} - E_s^{(0)}} \\ &= \frac{J^2}{4U}\left[\frac{k+1}{N-2k-1+\frac{\nu}{2U}} - \frac{k}{N-2k+1+\frac{\nu}{2U}}\right]\sqrt{n}\sqrt{m+1}. \end{aligned} \tag{A.7}$$

A.2 Initial state evolution

In this section, we derive the time evolution of the initial state used in the rotation sensing protocol presented in Section 4.4, given by

$$|\Psi(0)\rangle = |N,0,0,0\rangle = \frac{(a_1^\dagger)^N}{\sqrt{N!}}|0\rangle\,. \tag{A.8}$$

Using the effective Hamiltonian (3.57) in $U = \exp(-itH_{\text{eff}})$, we have

$$U|\Psi(0)\rangle = \frac{(Ua_1^\dagger\overbrace{U^\dagger U\ldots U^\dagger U}^{N-1\text{ times}}a_1^\dagger U^\dagger)}{\sqrt{N!}}U|0\rangle = \frac{(Ua_1^\dagger U^\dagger)^N}{\sqrt{N!}}|0\rangle\,. \tag{A.9}$$

From here, it's more convenient to evaluate $Ua_1^\dagger U^\dagger$ in terms of the normalized modes given by Equation (3.34). This can be done by applying the inverse transform

$$a_1^\dagger = \frac{1}{\sqrt{3}}(b_0^\dagger + b_+^\dagger + b_-^\dagger). \tag{A.10}$$

Using the identify

$$e^X Y e^{-X} = \sum_{n=0}^{\infty}\frac{[X,Y]_n}{n!} \tag{A.11}$$

where

$$[X,Y]_n \equiv \underbrace{[X,\cdots[X,[X,}_{n\text{ times}}\ Y]]\cdots]\,, \quad [X,Y]_0 \equiv Y, \tag{A.12}$$

we find:

$$\begin{aligned} Ub_0^\dagger U^\dagger &= \sum_{n=0}^{\infty}\frac{\left[-itH_{\text{eff}}, b_0^\dagger\right]_n}{n!} = \sum_{n=0}^{\infty}\frac{\left[it\left(c_+Q_+ + c_-Q_-\right), b_0^\dagger\right]_n}{n!} = b_0^\dagger, \\ Ub_+^\dagger U^\dagger &= \sum_{n=0}^{\infty}\frac{\left[-itH_{\text{eff}}, b_+^\dagger\right]_n}{n!} = \sum_{n=0}^{\infty}\frac{(itc_+)^n}{n!}b_+^\dagger = e^{itc_+}b_+^\dagger, \\ Ub_-^\dagger U^\dagger &= \sum_{n=0}^{\infty}\frac{\left[-itH_{\text{eff}}, b_-^\dagger\right]_n}{n!} = \sum_{n=0}^{\infty}\frac{(itc_-)^n}{n!}b_-^\dagger = e^{itc_-}b_-^\dagger. \end{aligned} \tag{A.13}$$

where we defined $c_\pm = \xi \pm \zeta$. Thus, we can write $Ua_1^\dagger U^\dagger$ as

$$Ua_1^\dagger U^\dagger = \frac{1}{\sqrt{3}}\left(b_0^\dagger + e^{itc_+}b_+^\dagger + e^{itc_-}b_-^\dagger\right) \tag{A.14}$$

Substituting $b_0^\dagger$, $b_+^\dagger$ and $b_-^\dagger$ for their full expressions in terms of $a_1^\dagger$, $a_2^\dagger$ and $a_3^\dagger$ in the above expression leads to

$$\begin{aligned} Ua_1^\dagger U^\dagger = \frac{1}{3}\Big[&a_1^\dagger + a_2^\dagger + a_3^\dagger \\ &+ e^{itc_+}\left(a_1^\dagger + \sigma a_2^\dagger + \sigma^{-1}a_3^\dagger\right) + e^{itc_-}\left(a_1^\dagger + \sigma^{-1}a_2^\dagger + \sigma a_3^\dagger\right)\Big], \end{aligned} \tag{A.15}$$

where $\sigma = \exp(2\pi i/3)$, which can be rearranged into

$$\begin{aligned} Ua_1^\dagger U^\dagger = \frac{1}{3}\Big(&\left[1 + 2e^{-it\xi}\cos(t\zeta)\right]a_1^\dagger + \left[1 + 2e^{-it\xi}\cos(t\zeta + 2\pi/3)\right]a_2^\dagger \\ &+ \left[1 + 2e^{-it\xi}\cos(t\zeta + 4\pi/3)\right]a_3^\dagger\Big). \end{aligned} \tag{A.16}$$

Substituting for above expression in the time evolution of the initial state results in the coherent state of Equation (4.23):

$$|\Psi(t)\rangle = \frac{\left[\sigma_1(t)\,a_1^\dagger + \sigma_2(t)\,a_2^\dagger + \sigma_3(t)\,a_3^\dagger\right]^N}{3^N\sqrt{N!}}|0\rangle \tag{A.17}$$

where $\sigma_j(t) = 1 + 2e^{-it\xi}\cos\theta_j(t)$ and $\theta_j(t) = t\zeta + 2\pi(j-1)/3$ for $j = 1, 2, 3$.

A.3 Outer site expectation values

In this section, we derive the analytical expressions for the expectation values of the outer site populations in the resonant regime, presented in Section 4.2. In order to facilitate the calculation of $\Delta(N_2 - N_3)$ in the next section, we evaluate $U^\dagger N_j U$ itself, found in

$$\langle N_j\rangle = \langle\Psi(t)|\,N_j\,|\Psi(t)\rangle = \langle\Psi(0)|\,U^\dagger N_j U\,|\Psi(0)\rangle, \tag{A.18}$$

instead of using the evolved state found in Equation (A.17). According to Equation (3.34), the number operators of the outer sites can be written as ($j = 1, 2, 3$)

$$\begin{aligned} N_j &= \frac{1}{3}\left(b_0^\dagger + \sigma^{-j+1}b_+^\dagger + \sigma^{j-1}b_-^\dagger\right)\left(b_0 + \sigma^{j-1}b_+ + \sigma^{-j+1}b_-\right) \\ &= \frac{1}{3}\left[Q_0 + Q_+ + Q_- + \sigma^{-j+1}\Gamma + \sigma^{j-1}\Gamma^\dagger\right] \end{aligned} \tag{A.19}$$

where

$$\Gamma \equiv b_0^\dagger b_- + b_-^\dagger b_+ + b_+^\dagger b_0. \tag{A.20}$$

Since $U^\dagger Q_m U = Q_m$, evaluating $U^\dagger\Gamma U$ is sufficient to derive $\langle N_j\rangle$. Using Equation (A.13), we have (note that $U^\dagger \to U$)

$$U^\dagger\Gamma U = e^{itc_-}b_0^\dagger b_- + e^{2it\zeta}b_-^\dagger b_+ + e^{-itc_+}b_+^\dagger b_0 \tag{A.21}$$

Substituting $b_0^\dagger$, $b_+^\dagger$ and $b_-^\dagger$ for their full expressions in terms of $a_1^\dagger$, $a_2^\dagger$ and $a_3^\dagger$ in the above expression leads to

$$\begin{aligned} U^\dagger\Gamma U = \frac{1}{3}\Big[&\left(e^{-itc_+} + e^{2it\zeta} + e^{itc_-}\right)N_1 \\ &+ \left(e^{itc_+} + \sigma^{-1}e^{2it\zeta} + \sigma e^{-itc_-}\right)a_2^\dagger a_1 + \left(\sigma e^{itc_+} + \sigma^{-1}e^{2it\zeta} + e^{-itc_-}\right)a_1^\dagger a_2 \\ &+ \left(e^{itc_+} + \sigma e^{2it\zeta} + \sigma^{-1}e^{-itc_-}\right)a_3^\dagger a_1 + \left(\sigma^{-1}e^{itc_+} + \sigma e^{2it\zeta} + e^{-itc_-}\right)a_1^\dagger a_3\Big] \\ &+ \cdots \end{aligned} \tag{A.22}$$

where $(\cdots)$ denotes terms that are not proportional to a_1 or $a_1^\dagger$. For the initial state $|\Psi(0)\rangle = |N,0,0,0\rangle$, all terms that are not proportional to N_1 in the above expression vanish, thus

$$\begin{aligned}\langle N_j\rangle &= \frac{1}{3}\langle\Psi(0)|\left[N_1+N_2+N_3+\sigma^{-j+1}U^\dagger\Gamma U+\sigma^{j-1}U^\dagger\Gamma^\dagger U\right]|\Psi(0)\rangle \\ &= \frac{N}{9}\left[3+\sigma^{-j+1}\left(e^{-itc_+}+e^{2it\zeta}+e^{itc_-}\right)+\sigma^{j-1}\left(e^{itc_+}+e^{-2it\zeta}+e^{-itc_-}\right)\right].\end{aligned} \tag{A.23}$$

Rearranging the above expression in terms of $\sigma = \exp(2\pi i/3)$ and $c_\pm = \xi \pm \zeta$, we recover Equation (4.24):

$$\langle N_j\rangle = \frac{N}{9}\left(1+4\cos\theta_j(t)\left[\cos(t\xi)+\cos\theta_j(t)\right]\right) \tag{A.24}$$

where $\theta_j(t) = t\zeta + 2\pi(j-1)/3$ for $j = 1,2,3$.

A.4 Error formula calculation

In order to find a closed expression for $\Delta(N_2-N_3)$, we need to evaluate both $\mathcal{O}(t) \equiv U^\dagger(N_2-N_3)U$ and $\mathcal{O}^2(t) = U^\dagger(N_2-N_3)^2U$. According to Equation (A.19), the imbalance between sites 2 and 3 can be written as

$$N_2-N_3 = -\frac{1}{3}\left(\sigma-\sigma^{-1}\right)\left(\Gamma-\Gamma^\dagger\right) = -\frac{i}{\sqrt{3}}\left(\Gamma-\Gamma^\dagger\right). \tag{A.25}$$

Substituting for Equation (A.22) in the above expression, we obtain the relevant terms

$$\begin{aligned}\mathcal{O}(t) &= I(t)N_1 \\ &\quad + \frac{i}{3\sqrt{3}}\left(Aa_2^\dagger a_1 + A^*a_1^\dagger a_2 + Ba_3^\dagger a_1 + B^*a_1^\dagger a_3\right)+\cdots\end{aligned} \tag{A.26}$$

and

$$\mathcal{O}^2(t) = I^2(t)N_1^2 + \frac{1}{27}\left(|A|^2+|B|^2\right)N_1+\cdots \tag{A.27}$$

where

$$I(t) = \frac{2}{3\sqrt{3}}\left[\sin(2\zeta t)-2\sin(\zeta t)\cos(\xi t)\right], \tag{A.28}$$

$$A = e^{-itc_+}-e^{-itc_-}+\sigma\left(e^{-2it\zeta}-e^{-itc_+}\right)+\sigma^{-1}\left(e^{2it\zeta}+e^{-itc_-}\right), \tag{A.29}$$

$$B = e^{-itc_+}-e^{-itc_-}+\sigma^{-1}\left(e^{-2it\zeta}-e^{-itc_+}\right)+\sigma\left(e^{2it\zeta}+e^{-itc_-}\right). \tag{A.30}$$

For the initial state $|\Psi(0)\rangle = |N,0,0,0\rangle$, we obtain

$$\langle N_2-N_3\rangle = I(t)N = \frac{2N}{3\sqrt{3}}\left[\sin(2\zeta t)-2\sin(\zeta t)\cos(\xi t)\right] \tag{A.31}$$

and

$$\langle(N_2-N_3)^2\rangle = I^2(t)N^2 + G(t)N \tag{A.32}$$

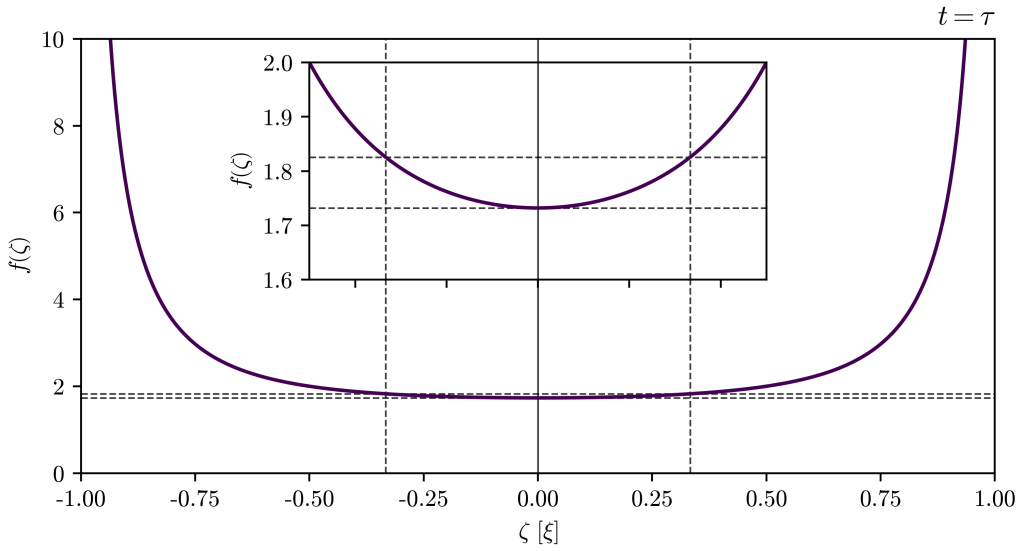

Figure A.1: Plots of Equation (A.37) as a function of ζ. The vertical dashed lines represent $|\zeta| \leq \zeta_{\max}$. The horizontal dashed lines represent $\sqrt{3} \leq f(\zeta) \leq \sqrt{3+1/3}$.

where

$$\begin{aligned} G(t) &= \frac{1}{27}\left(|A|^2 + |B|^2\right) \\ &= \frac{2}{27}\left(-\cos\left[t(\zeta-\xi)\right] + \cos\left[2t(\zeta-\xi)\right] - 2\cos\left[t(3\zeta-\xi)\right]\right. \\ &\quad - \cos\left[t(\zeta+\xi)\right] + \cos\left[2t(\zeta-\xi)\right] - 2\cos\left[t(3\zeta+\xi)\right] \\ &\quad \left. - \cos(2\zeta t) + \cos(4\zeta t) - 2\cos(2\xi t) + 6\right). \end{aligned} \tag{A.33}$$

Since step (iii) of the rotation sensing protocol presented in Section 4.4 requires measurements be taken at $t = \tau = \pi/\xi$, we have

$$\langle N_2 - N_3\rangle|_{t=\tau} = \frac{2N}{3\sqrt{3}}\left[\sin(2\pi\zeta/\xi) + 2\sin(\pi\zeta/\xi)\right] \tag{A.34}$$

and

$$\begin{aligned} \Delta(N_2 - N_3)|_{t=\tau} &= \sqrt{\langle \mathcal{O}^2(\pi/\xi)\rangle - \langle \mathcal{O}(\pi/\xi)\rangle^2} = \sqrt{G(\pi/\xi)\,N} \\ &= \sqrt{\frac{8N}{27}}\sqrt{2+\cos\left(\frac{\pi\zeta}{\xi}\right)}\cos\left(\frac{3\pi\zeta}{2\xi}\right). \end{aligned} \tag{A.35}$$

Substituting for Equations (A.34) and (A.35) in the error propagation formula, we recover Equation (4.32):

$$\delta\Omega = \frac{\Delta(N_2 - N_3)}{|\partial_\Omega\langle N_2 - N_3\rangle|} = \frac{f(\zeta)}{2\tau W\sqrt{2N}} \tag{A.36}$$

where

$$f(\zeta) = \sqrt{2+\cos\left(\frac{\pi\zeta}{\xi}\right)}\sec\left(\frac{\pi\zeta}{2\xi}\right) \tag{A.37}$$

is a smooth and convex curve with little variation ($\sqrt{3} \leq f(\zeta) \leq \sqrt{3+1/3}$) in the interval $0 \leq \zeta \leq \zeta_{\max}$, as seen in Figure A.1.

Bibliography

[1]A. Einstein, "Quantentheorie des einatomigen idealen gases", in *Albert einstein: akademie-vorträge* (John Wiley & Sons, Ltd, 2005), pp. 237–244.

[2]A. Einstein, "Quantentheorie des einatomigen idealen gases. zweite abhandlung", in , Vol. 23 (Aug. 2006), pp. 245–257.

[3]Bose, "Plancks gesetz und lichtquantenhypothese", Zeitschrift für Physik **26**, 178–181 (1924).

[4]M. H. Anderson, J. R. Ensher, M. R. Matthews, C. E. Wieman, and E. A. Cornell, "Observation of bose-einstein condensation in a dilute atomic vapor", Science **269**, 198–201 (1995).

[5]K. B. Davis, M. .-. Mewes, M. R. Andrews, N. J. van Druten, D. S. Durfee, D. M. Kurn, and W. Ketterle, "Bose-einstein condensation in a gas of sodium atoms", Phys. Rev. Lett. **75**, 3969–3973 (1995).

[6]S. Inouye, M. R. Andrews, J. Stenger, H.-J. Miesner, D. M. Stamper-Kurn, and W. Ketterle, "Observation of feshbach resonances in a bose–einstein condensate", Nature **392**, 151–154 (1998).

[7]E. A. Donley, N. R. Claussen, S. L. Cornish, J. L. Roberts, E. A. Cornell, and C. E. Wieman, "Dynamics of collapsing and exploding bose–einstein condensates", Nature **412**, 295–299 (2001).

[8]M. Greiner, O. Mandel, T. Esslinger, T. W. Hänsch, and I. Bloch, "Quantum phase transition from a superfluid to a mott insulator in a gas of ultracold atoms", Nature **415**, 39–44 (2002).

[9]F. Dalfovo, S. Giorgini, L. P. Pitaevskii, and S. Stringari, "Theory of bose-einstein condensation in trapped gases", Rev. Mod. Phys. **71**, 463–512 (1999).

[10]N. P. Proukakis and B. Jackson, "Finite-temperature models of bose-einstein condensation", Journal of Physics B: Atomic, Molecular and Optical Physics **41**, 203002 (2008).

[11]H. A. Gersch and G. C. Knollman, "Quantum cell model for bosons", Phys. Rev. **129**, 959–967 (1963).

[12]J. Hubbard, "Electron correlations in narrow energy bands", Proceedings of the Royal Society of London. Series A. Mathematical and Physical Sciences **276**, 238–257 (1963).

[13]D. Jaksch, C. Bruder, J. I. Cirac, C. W. Gardiner, and P. Zoller, "Cold bosonic atoms in optical lattices", Phys. Rev. Lett. **81**, 3108–3111 (1998).

[14]M. Greiner, O. Mandel, T. W. Hänsch, and I. Bloch, "Collapse and revival of the matter wave field of a bose–einstein condensate", Nature **419**, 51–54 (2002).

[15]O. Jürgensen, F. Meinert, M. J. Mark, H.-C. Nägerl, and D.-S. Lühmann, "Observation of density-induced tunneling", Phys. Rev. Lett. **113**, 193003 (2014).

[16]S. Baier, M. J. Mark, D. Petter, K. Aikawa, L. Chomaz, Z. Cai, M. Baranov, P. Zoller, and F. Ferlaino, "Extended bose-hubbard models with ultracold magnetic atoms", Science **352**, 201–205 (2016).

[17]O. Dutta, M. Gajda, P. Hauke, M. Lewenstein, D.-S. Lühmann, B. A. Malomed, T. Sowiński, and J. Zakrzewski, "Non-standard hubbard models in optical lattices: a review", Reports on Progress in Physics **78**, 066001 (2015).

[18]T. Chanda, L. Barbiero, M. Lewenstein, M. J. Mark, and J. Zakrzewski, "Recent progress on quantum simulations of non-standard bose-hubbard models", Reports on Progress in Physics **88**, 044501 (2025).

[19]R. Grimm, M. Weidemüller, and Y. B. Ovchinnikov, "Optical dipole traps for neutral atoms", in , Vol. 42, edited by B. Bederson and H. Walther, Advances In Atomic, Molecular, and Optical Physics (Academic Press, 2000), pp. 95–170.

[20]P. Windpassinger and K. Sengstock, "Engineering novel optical lattices", Reports on Progress in Physics **76**, 086401 (2013).

[21]J. Links, A. Foerster, A. P. Tonel, and G. Santos, "The two-site bose–hubbard model", Annales Henri Poincaré **7**, 1591–1600 (2006).

[22]L. H. Ymai, A. P. Tonel, A. Foerster, and J. Links, "Quantum integrable multi-well tunneling models", Journal of Physics A: Mathematical and Theoretical **50**, 264001 (2017).

[23]K. W. Wilsmann, L. H. Ymai, A. P. Tonel, J. Links, and A. Foerster, "Control of tunneling in an atomtronic switching device", Communications Physics **1**, 91 (2018).

[24]D. S. Grün, K. Wittmann W., L. H. Ymai, J. Links, and A. Foerster, "Protocol designs for noon states", Communications Physics **5**, 36 (2022).

[25]K. W. W., L. H. Ymai, B. H. C. Barros, J. Links, and A. Foerster, "Controlling entanglement in a triple-well system of dipolar atoms", Phys. Rev. A **108**, 033313 (2023).

[26]L. H. Ymai and A. P. Tonel, "Tunneling control of dipolar bosons in triple-well circuits via dipole polarization orientation and quantum sensing application", Phys. Rev. A **112**, 013302 (2025).

[27]L. H. Ymai, K. Wittmann Wilsmann, A. P. Tonel, A. Foerster, and J. Links, "High-fidelity transfer of entangled states on a quantum turntable", Newton **1**, `10.1016/j.newton.2025.100226` (2025).

[28]K. Wittmann W., L. H. Ymai, G. S. Neto, and A. Foerster, "Atomtronic routing of dipolar bosons in a four-well star potential", Phys. Rev. A **113**, 023308 (2026).

[29]J. Maillet and V. Terras, "On the quantum inverse scattering problem", Nuclear Physics B **575**, 627–644 (2000).

[30]A. L. Retore, "Introduction to classical and quantum integrability", Journal of Physics A: Mathematical and Theoretical **55**, 173001 (2022).

[31]L. H. Ymai, K. W. Wilsmann, J. B. Neves, A. P. Tonel, J. Links, and A. Foerster, *Supersensitive rotation sensor from superintegrability*, 2026.

[32]T. Lahaye, T. Pfau, and L. Santos, "Mesoscopic ensembles of polar bosons in triple-well potentials", Phys. Rev. Lett. **104**, 170404 (2010).

[33]G. Pascoli, "The sagnac effect and its interpretation by paul langevin", Comptes Rendus Physique **18**, Science in the making: The Comptes rendus de l'Académie des sciences throughout history, 563–569 (2017).

[34]M. Baranov, "Theoretical progress in many-body physics with ultracold dipolar gases", Physics Reports **464**, 71–111 (2008).

[35]R. Bhat, "Bosons in rotating optical lattices", (2008).

[36]K. Góral, L. Santos, and M. Lewenstein, "Quantum phases of dipolar bosons in optical lattices", Phys. Rev. Lett. **88**, 170406 (2002).

[37]T. Lahaye, C. Menotti, L. Santos, M. Lewenstein, and T. Pfau, "The physics of dipolar bosonic quantum gases", Reports on Progress in Physics **72**, 126401 (2009).

[38]P. Davis, *Circulant matrices*, Monographs and textbooks in pure and applied mathematics (Wiley, 1979).

[39]A. J. Leggett, "Bose-einstein condensation in the alkali gases: some fundamental concepts", Rev. Mod. Phys. **73**, 307–356 (2001).

[40]G. Santos, A. Tonel, A. Foerster, and J. Links, "Classical and quantum dynamics of a model for atomic-molecular bose-einstein condensates", Phys. Rev. A **73**, 023609 (2006).

[41]L. Landau and E. Lifshitz, *Quantum mechanics: non-relativistic theory*, Teoreticheskaia fizika (Pergamon, 2013).

[42]L. Mandelstam and I. Tamm, "The uncertainty relation between energy and time in non-relativistic quantum mechanics", in *Selected papers*, edited by B. M. Bolotovskii, V. Y. Frenkel, and R. Peierls (Springer Berlin Heidelberg, Berlin, Heidelberg, 1991), pp. 115–123.

[43]S. Boixo, A. Datta, M. J. Davis, A. Shaji, A. B. Tacla, and C. M. Caves, "Quantum-limited metrology and bose-einstein condensates", Phys. Rev. A **80**, 032103 (2009).

[44]S. Boixo, S. T. Flammia, C. M. Caves, and J. Geremia, "Generalized limits for single-parameter quantum estimation", Phys. Rev. Lett. **98**, 090401 (2007).

[45]S. L. Braunstein and C. M. Caves, "Statistical distance and the geometry of quantum states", Phys. Rev. Lett. **72**, 3439–3443 (1994).

[46]S. L. Braunstein, C. M. Caves, and G. Milburn, "Generalized uncertainty relations: theory, examples, and lorentz invariance", Annals of Physics **247**, 135–173 (1996).

[47]*Quantum detection and estimation theory*, Mathematics in Science and Engineering (Academic Press, 1976).

[48]A. Kholevo, *Probabilistic and statistical aspects of quantum theory*, North-Holland series in statistics and probability (North-Holland Publishing Company, 1982).

[49]V. Giovannetti, S. Lloyd, and L. Maccone, "Quantum metrology", Phys. Rev. Lett. **96**, 010401 (2006).

[50]H. Lee, P. Kok, and J. P. Dowling, "A quantum rosetta stone for interferometry", Journal of Modern Optics **49**, 2325–2338 (2002).

[51]B. Yurke, S. L. McCall, and J. R. Klauder, "Su(2) and su(1,1) interferometers", Phys. Rev. A **33**, 4033–4054 (1986).

[52]V. Giovannetti, S. Lloyd, and L. Maccone, "Quantum-enhanced positioning and clock synchronization", Nature **412**, 417–419 (2001).

[53]S. Boixo, A. Datta, M. J. Davis, S. T. Flammia, A. Shaji, and C. M. Caves, "Quantum metrology: dynamics versus entanglement", Phys. Rev. Lett. **101**, 040403 (2008).

[54]M. Zwierz, C. A. Pérez-Delgado, and P. Kok, "General optimality of the heisenberg limit for quantum metrology", Phys. Rev. Lett. **105**, 180402 (2010).

[55]M. Napolitano, M. Koschorreck, B. Dubost, N. Behbood, R. J. Sewell, and M. W. Mitchell, "Interaction-based quantum metrology showing scaling beyond the heisenberg limit", Nature **471**, 486–489 (2011).

[56]R. J. Sewell, M. Napolitano, N. Behbood, G. Colangelo, F. Martin Ciurana, and M. W. Mitchell, "Ultrasensitive atomic spin measurements with a nonlinear interferometer", Phys. Rev. X **4**, 021045 (2014).

[57]S. Pang and A. N. Jordan, "Optimal adaptive control for quantum metrology with time-dependent hamiltonians", Nature Communications **8**, 14695 (2017).

[58]J. M. Boss, K. S. Cujia, J. Zopes, and C. L. Degen, "Quantum sensing with arbitrary frequency resolution", Science **356**, 837–840 (2017).

[59]M. Naghiloo, A. N. Jordan, and K. W. Murch, "Achieving optimal quantum acceleration of frequency estimation using adaptive coherent control", Phys. Rev. Lett. **119**, 180801 (2017).

[60]M. M. Rams, P. Sierant, O. Dutta, P. Horodecki, and J. Zakrzewski, "At the limits of criticality-based quantum metrology: apparent super-heisenberg scaling revisited", Phys. Rev. X **8**, 021022 (2018).

[61]T. Gefen, A. Rotem, and A. Retzker, "Overcoming resolution limits with quantum sensing", Nature Communications **10**, 4992 (2019).

[62]Z. Hou, Y. Jin, H. Chen, J.-F. Tang, C.-J. Huang, H. Yuan, G.-Y. Xiang, C.-F. Li, and G.-C. Guo, ""super-heisenberg" and heisenberg scalings achieved simultaneously in the estimation of a rotating field", Phys. Rev. Lett. **126**, 070503 (2021).

[63]M. J. W. Hall and H. M. Wiseman, "Does nonlinear metrology offer improved resolution? answers from quantum information theory", Phys. Rev. X **2**, 041006 (2012).

[64]B. Canuel, F. Leduc, D. Holleville, A. Gauguet, J. Fils, A. Virdis, A. Clairon, N. Dimarcq, C. J. Bordé, A. Landragin, and P. Bouyer, "Six-axis inertial sensor using cold-atom interferometry", Phys. Rev. Lett. **97**, 010402 (2006).

[65]A. Gauguet, B. Canuel, T. Lévèque, W. Chaibi, and A. Landragin, "Characterization and limits of a cold-atom sagnac interferometer", Phys. Rev. A **80**, 063604 (2009).

[66]G. Tackmann, P. Berg, C. Schubert, S. Abend, M. Gilowski, W. Ertmer, and E. M. Rasel, "Self-alignment of a compact large-area atomic sagnac interferometer", New J. Phys. **14**, 015002 (2012).

[67]C. L. Garrido Alzar, "Compact chip-scale guided cold atom gyrometers for inertial navigation: enabling technologies and design study", AVS Quantum Science **1**, 014702 (2019).

[68]C. Janvier, V. Ménoret, B. Desruelle, S. Merlet, A. Landragin, and F. Pereira dos Santos, "Compact differential gravimeter at the quantum projection-noise limit", Phys. Rev. A **105**, 022801 (2022).

[69]M. J. Wright, L. Anastassiou, C. Mishra, J. M. Davies, A. M. Phillips, S. Maskell, and J. F. Ralph, "Cold atom inertial sensors for navigation applications", Frontiers in Physics **Volume 10 - 2022**, 10.3389/fphy.2022.994459 (2022).

[70]O. Adeniji, C. Henry, S. Thomas, R. C. Sapp, A. Goyal, C. W. Clark, and M. Edwards, *Double-target bec atomtronic rotation sensor*, 2024.

[71]K. S. Hardman, P. B. Wigley, P. J. Everitt, P. Manju, C. C. N. Kuhn, and N. P. Robins, "Time-of-flight detection of ultra-cold atoms using resonant frequency modulation imaging", Opt. Lett. **41**, 2505–2508 (2016).

[72]P. B. Wigley, P. J. Everitt, K. S. Hardman, M. R. Hush, C. H. Wei, M. A. Sooriyabandara, P. Manju, J. D. Close, N. P. Robins, and C. C. N. Kuhn, "Non-destructive shadowgraph imaging of ultra-cold atoms", Opt. Lett. **41**, 4795–4798 (2016).

[73]P. Wigley, "Generating and observing soliton dynamics in bose einstein condensates", PhD thesis (Jan. 2017).